

Tensor network state approach to quantum topological phase transitions and their criticalities of \mathbb{Z}_2 topologically ordered states

Wen-Tao Xu¹ and Guang-Ming Zhang^{1,2}

¹*State Key Laboratory of Low-Dimensional Quantum Physics and
Department of Physics, Tsinghua University, Beijing 100084, China.*

²*Collaborative Innovation Center of Quantum Matter, Beijing 100084, China.*

(Dated: September 24, 2018)

Due to the absence of local order parameters, it is a challenging task to characterize the quantum topological phase transitions between topologically ordered phases in two dimensions. In this paper, we construct a topologically ordered tensor network wavefunction with one parameter λ , describing both the toric code state ($\lambda = 1$) and double semion state ($\lambda = -1$). Via calculating the correlation length defined from the one-dimensional quantum transfer operator of the wave function norm, we can map out the complete phase diagram in terms of the parameter λ and three different quantum critical points (QCPs) at $\lambda = 0, \pm 1.73$ are identified. The first one separates the toric code phase and double semion phase, while later two describe the topological phase transitions from the toric code phase or double semion phase to the symmetry breaking phase, respectively. When mapping the quantum tensor network wavefunction to the exactly solved statistical model, the norm of the wave function is identified as the partition function of the classical eight-vertex model, and both QCPs at $\lambda = \pm 1.73$ correspond to the eight-vertex model at the critical point $\lambda = \sqrt{3}$, while the QCP at $\lambda = 0$ corresponds to the critical six-vertex model. Actually such a quantum-classical mapping can not yield the complete low-energy excitations at these three QCPs. We further demonstrate that the full eigenvalue spectra of the transfer operators without/with the flux insertions can give rise to the complete quantum criticalities, which are described by the (2+0)-dimensional free boson conformal field theories (CFTs) compactified on a circle with the radius $R = \sqrt{6}$ at $\lambda = \pm\sqrt{3}$ and $R = \sqrt{8/3}$ at $\lambda = 0$. From the complete transfer operator spectra, the finite-size spectra of the CFTs for the critical eight-vertex model are obtained, and the topological sectors of anyonic excitations are yielded as well. Furthermore, for the QCP at $\lambda = 0$, no anyon condensation occurs, but the emerged symmetries of the matrix product operators significantly enrich the topological sectors of the CFT spectra. Finally, we provide our understanding on the (2+0)-dimensional conformal quantum criticalities and their possible connection with the generic (2+1)-dimensional CFTs for quantum topological phase transitions.

I. INTRODUCTION

Topological phases of matter and topological order become two important novel concepts in current condensed matter physics. In the past decade, the theoretical framework for topological order in two dimensions has been gradually established. For example, some exactly solvable models with topological orders have been constructed^{1,2}, a physical picture for understanding generic non-chiral topologically ordered states has been proposed³, the fixed-point wave functions for arbitrary non-chiral topological order are formulated in terms of tensor networks⁴, and the profound underlying mathematics classifying the topological ordered phases have also been unveiled⁵. Albeit so many inspiring successes for understanding of topologically ordered phases are achieved, the topological phase transitions among these topologically ordered phases are still lack of a unified theoretical description. Moreover, the anyon condensation mechanism provides us a physical picture for some topological phase transitions⁶, however, it can not be generalized to characterize all kinds of topological phase transitions. So it is urgent to develop a systematic theoretical framework for quantum topological phase transitions.

The defining feature of topologically ordered phases is the ground state degeneracy that depends on the topol-

ogy of the manifold in which the systems live. Other important properties, such as the topological entanglement entropy and braiding statistics of anyons, can be extracted from the ground state wave functions as well⁷. It is generally believed that almost all information about the topologically ordered phase is encoded in the ground states. But a generic ground state wave function of the interacting many-body systems is an entangled complex which is hard to be obtained. However, the majority of many-body physical ground states satisfy the area law theorem, the corresponding wavefunctions can be efficiently expressed in terms of tensor network states⁸. With such tensor network states, many properties of the topological phases, such as entanglement entropy, entanglement spectrum⁹, modular matrices¹⁰ and all kinds of expectation values, can be efficiently calculated numerically. In one dimension, from the exact ground-state wave functions in the matrix product state representation, we have successfully decoded the quantum criticalities of the topological phase transitions from the symmetry protected topological (SPT) phases to their adjacent trivial phase with the same symmetry¹¹⁻¹⁴.

For the non-chiral topologically ordered tensor network states in two dimensions, the central object is the matrix product operator (MPO), which acts on the virtual (auxiliary) degrees of freedom of the tensor networks^{15,16}.

The insertion of a MPO in the tensor network states on a torus can transform the topological ground state into its degenerate ground state, just like the “Wilson loop” operator. Actually we can use these MPOs to determine the anyonic excitations contained in the topologically ordered tensor network states¹⁵. In principle, by properly parameterizing the local tensors with a finite bond dimension, the tensor network state wave function can characterize various topological ordered phases and even the quantum critical points. Such a tensor network state approach is thus more useful than directly studying the topological phase transitions from the parameterized model Hamiltonian, because solving a quantum Hamiltonian with local interactions is usually more difficult particular in two dimensions.

In this paper, we start from a two-dimensional tensor network wave function for \mathbb{Z}_2 SPT phases with a tuning parameter λ (Ref.¹⁷), where the protecting \mathbb{Z}_2 symmetry is defined by the MPO of the tensor network. By introducing \mathbb{Z}_2 gauge degrees of freedom into the \mathbb{Z}_2 SPT tensor network state, we can construct a parameterized tensor network wave function with \mathbb{Z}_2 topological orders, which incorporates the toric code phase, double semion phase, the symmetry breaking phase, as well as the phase transition points between these phases. Via calculating the correlation length from the one-dimensional quantum transfer operator of the wave function norm, we can map out the complete phase diagram and identify three different quantum critical points (QCPs) at $\lambda = 0, \pm 1.73$, respectively. The first one separates the toric code phase ($0 < \lambda < 1.73$) and the double semion phase ($-1.73 < \lambda < 0$), while later two describe the topological phase transitions from the toric code or double semion phase to the symmetry breaking phase ($|\lambda| > 1.73$), respectively. Moreover, this one parameter family of tensor network wave function can be mapped into the partition function of the exactly solved eight-vertex model, where the phases with negative parameter λ merge into those phases with positive parameter λ . Then the double semion phase becomes equivalent to the toric code phase, and the QCPs at $\lambda \simeq \pm 1.73$ correspond to the critical point $\lambda = \sqrt{3}$ of the eight-vertex model. But the QCP at $\lambda = 0$ corresponds to the critical six-vertex model, a special critical point of the eight-vertex model.

In order to investigate the complete quantum criticalities associated to the topological phase transitions, the full spectra of the transfer operators without/with the flux insertion are carefully analyzed at these three QCPs separately, and we find that the static correlators at all these three QCPs are characterized by the two-dimensional free boson conformal field theory (CFT) compactified on a circle with compactified radii: $R = \sqrt{6}$ for QCPs at $\lambda = \pm\sqrt{3}$ and $R = \sqrt{8/3}$ for QCP at $\lambda = 0$. Moreover, the phase transitions at $\lambda = \pm\sqrt{3}$ can be related to the anyon condensation in the tensor network formalism^{18–21}, and the finite-size spectrum of the critical eight-vertex model corresponds to the charge 1 sector, while the sector of charge -1 exhibits the condensa-

tion of topological anyon excitations. However, the QCP between two topologically ordered phases at $\lambda = 0$ is quite unusual, where the transfer operators without/with flux insertion acquire additional MPO symmetries. Thus there is a significant enrichment in the structure of CFT spectra with fractionalized anyonic excitations. Finally, we provide our understanding on such (2+0)-dimensional conformal quantum criticalities for quantum topological phase transitions in two dimensions^{22,23}.

This paper is organized as follows. In Sec.II, we construct the one parameter family of tensor network wave function with two distinct \mathbb{Z}_2 topological orders in two dimensions. In Sec.III, the one-dimensional quantum transfer operator is introduced from the tensor network wave function norm, and from the calculations of the correlation length the complete phase diagram is mapped out and three different QCPs are identified. In Sec.IV, the quantum-classical correspondence is carefully discussed and the positions of those QCPs are confirmed from the exactly solved statistical models. In Sec.V, to fully derive the spectra of the CFTs of these three QCPs, we carefully analyze the complete spectra of the transfer operators without/with the flux insertions. Sec.VI provides our understanding of the (2+0)-dimensional conformal QCPs, and their relationship with the generic (2+1)-dimensional CFTs for quantum topological phase transitions. Some related discussions are included in the Appendices.

II. TENSOR-NETWORK WAVE FUNCTIONS

A. Wave functions for the \mathbb{Z}_2 SPT phases

According to the classification theory for SPT phases in two dimensions²⁴, there exist two topologically distinct SPT phases protected by \mathbb{Z}_2 symmetry, one is trivial SPT phase and the other is non-trivial SPT phase^{25,26}. The fixed-point wave functions of these two phases can be represented in terms of the double line tensor networks on a two-dimensional square lattice^{4,25}, as shown in Fig. 1. Both physical and virtual degrees of freedom are \mathbb{Z}_2 spins. The physical indices of local tensor $\tilde{\mathcal{A}}$ are denoted by the small circles, and a single lattice site represented by the big circle. Four neighboring \mathbb{Z}_2 spins in the same inter-site plaquette (the blue square in Fig. 1) are locked in the GHZ state $|0000\rangle + |1111\rangle$. Each local tensor $\tilde{\mathcal{A}}$ in Fig. 1(a) has eight virtual indices ($u, u', r, r', d, d', l, l'$) and four physical indices ($s_\alpha, s_\beta, s_\gamma, s_\delta$), and is given by

$$\tilde{\mathcal{A}}_{u'r'r'u'u'dd'}^{s_\alpha s_\beta s_\gamma s_\delta} = A^{s_\alpha s_\beta s_\gamma s_\delta} \delta_{lu}^{s_\alpha} \delta_{u'r'}^{s_\beta} \delta_{r'd'}^{s_\gamma} \delta_{l'd}^{s_\delta}, \quad (1)$$

where $\delta_{jk}^i = 1$ for $i = j = k$ and $\delta_{jk}^i = 0$ otherwise. Because the entangled plaquettes are considered, the construction of double line tensor network states intrinsically differs from the construction of projected entangled pair states⁸, where only entangled pair states are considered. Different tensor network wave functions are determined

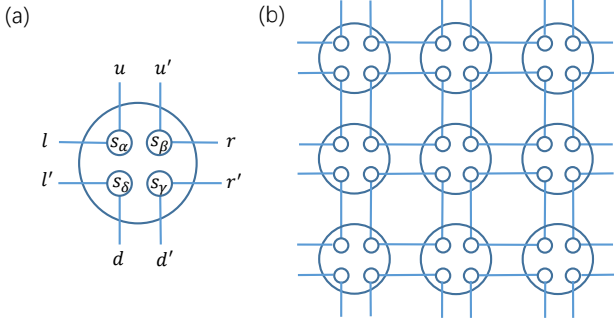


FIG. 1: (a) The structure of local tensor. (b) The SPT tensor network state.

by the choices of $A^{s_\alpha s_\beta s_\gamma s_\delta}$. So the tensor network state is expressed by contracting all adjacent local tensors:

$$|\psi(\lambda)\rangle = \sum_{\{s_\alpha\}} \text{tTr}(\tilde{\mathcal{A}} \otimes \cdots \otimes \tilde{\mathcal{A}}) |s_1 s_2 s_3 \cdots\rangle, \quad (2)$$

where tTr denotes the tensor contraction over all virtual indices and $\{s_\alpha\}$ are all spin configurations. It has been proven that the tensor network states can generally have a parent Hamiltonian as the summation of local commuting projectors²⁷, so our the tensor network state can be regarded as the ground state of a two-dimensional quantum systems with local interactions.

The main difference between the trivial and non-trivial SPT phases reflects in the MPO representation of the on-site protecting symmetry on the virtual space. For simplicity, the on-site protecting \mathbb{Z}_2 symmetry is chosen as $\prod X^{\otimes 4}$, where $X^{\otimes 4}$ is the four Pauli operators σ^x acting on the four spins on the same site. As shown in Fig.2, the protecting symmetry acting on the physical degrees of freedom is equivalent to the MPO symmetry acting on the virtual degrees of freedom¹⁶. Note that the MPO representations of the on-site symmetry on the virtual space are not unique, so we just follow the conventional expression used in Ref.²⁵. For the trivial SPT phase, the MPO is trivial in the sense that the bond dimension of the MPO is one, so it can be expressed as direct product of local operators: $U_x = \prod_{j=1}^4 X_j^{\otimes 2}$, where $X_j^{\otimes 2}$ acts on the j -th quarter plaquette and the product runs over four adjacent quarter plaquettes shown in Fig.2(a). However, the bond dimension of MPO for the non-trivial SPT phase is greater than one, and it is a non-on-site operator given by²⁵

$$U_{\text{czz}} = \prod_{j=1}^4 X_j^{\otimes 2} \prod_{j=1}^4 CZ_{j,j+1}, \quad (3)$$

where $X_j^{\otimes 2}$ acts on the j -th quarter plaquette and $CZ_{j,j+1} = \text{diag}(1, 1, 1, -1)$ is the control-Z gate acting on the j -th and $(j+1)$ -th quarter plaquettes. When a quarter plaquette is grouped as a single degree of freedom, one can find that the bond dimension of U_{czz} is indeed

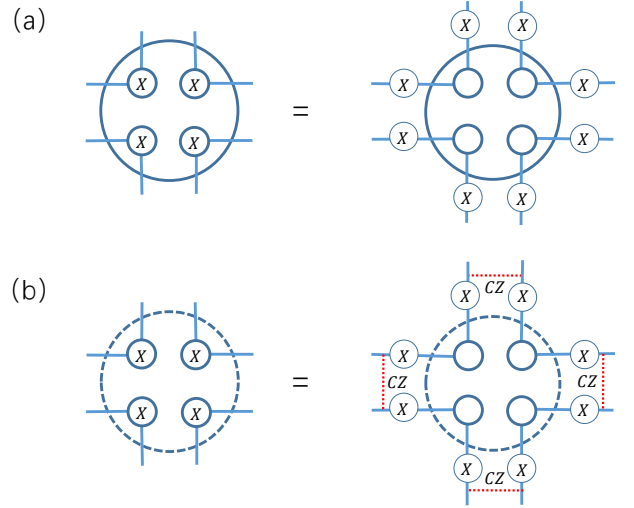


FIG. 2: Acting the on-site symmetry $X^{\otimes 4}$ on the physical degrees of freedom is equivalent to acting MPO symmetry on the virtual degrees of freedom. (a) The MPO for the local tensor $\tilde{\mathcal{A}}$ of the trivial SPT state. (b) The MPO for local tensor of the nontrivial SPT state.

two. To satisfy the requirements of Fig.2, the following constraints on the local tensor have to be imposed:

$$\begin{aligned} A^{0000} &= A^{1111}, A^{0001} = A^{1110}, \\ A^{0010} &= A^{1101}, A^{0011} = A^{1100}, \\ A^{0100} &= A^{1011}, A^{0101} = A^{1010}, \\ A^{0110} &= A^{1001}, A^{0111} = A^{1000}, \end{aligned} \quad (4)$$

for the trivial SPT phase, and

$$\begin{aligned} A^{0000} &= A^{1111}, A^{0001} = A^{1110}, \\ A^{0010} &= A^{1101}, A^{0011} = -A^{1100}, \\ A^{0100} &= A^{1011}, A^{0110} = -A^{1001}, \\ A^{0101} &= A^{1010}, A^{0111} = A^{1000}, \end{aligned} \quad (5)$$

for non-trivial SPT phase. Thus, it is the MPO symmetry that we can use to distinguish the trivial or nontrivial SPT phases.

For convenience, the simplest local tensor A for the trivial SPT tensor network state is chosen as

$$A^{s_\alpha s_\beta s_\gamma s_\delta} = 1, \text{ for all } s_\alpha s_\beta s_\gamma s_\delta, \quad (6)$$

while for non-trivial SPT tensor network state the local tensor is

$$A^{0011} = A^{0110} = -1; A^{s_\alpha s_\beta s_\gamma s_\delta} = 1, \text{ otherwise.} \quad (7)$$

Actually, these two tensor network states represent the fixed points of the trivial and nontrivial SPT phases, respectively. More importantly, we can construct a one parameter family of tensor network state with a dimensionless tuning parameter λ in the local tensor:

$$\begin{aligned} A^{0011} &= A^{0110} = \lambda, \\ A^{1100} &= A^{1001} = |\lambda|, \\ A^{s_\alpha s_\beta s_\gamma s_\delta} &= 1, \text{ otherwise,} \end{aligned} \quad (8)$$

to incorporate both fixed-point wave functions $\lambda = \pm 1$ simultaneously¹⁷.

Moreover, for the general tensor network states, there exists a unitary transformation

$$W = \prod_{s_\alpha s_\beta s_\gamma s_\delta} \sum_{s_\alpha s_\beta s_\gamma s_\delta} w(s_\alpha s_\beta s_\gamma s_\delta) |s_\alpha s_\beta s_\gamma s_\delta\rangle \langle s_\alpha s_\beta s_\gamma s_\delta|, \quad (9)$$

with $w(0011) = w(0110) = -1$ and $w(s_\alpha s_\beta s_\gamma s_\delta) = 1$ otherwise. Under this transformation, the tensor-network state $|\psi(\lambda)\rangle$ is changed into $|\psi(-\lambda)\rangle$. Since such a transformation plays the role of a duality transformation, $\lambda = 0$ becomes a self-dual point and the wave function $|\psi(0)\rangle$ is invariant under this transformation. If the protecting symmetries are preserved in the parameter space, tuning the parameter λ from 1 to -1 , one can encounter a topological quantum phase transition point between these two SPT phases. Exactly at the transition point, the critical tensor network state has both MPO representations of U_x and U_{zx} .

Since those four spins in the same inter-site plaquette are locked with each other, we can group the inter-site plaquette as a single spin located at the vertices of the red lattice in Fig. 3(a). When $|\lambda| \gg 1$, there only leave four dominant elements in the local tensor $A^{s_\alpha s_\beta s_\gamma s_\delta}$, which form four different degenerate ground states configurations for an arbitrary system size, corresponding to the spontaneous symmetry breaking phase with the stripe ferromagnetic order, as shown in Fig.3 (b). Because the \mathbb{Z}_2 SPT phases and symmetry breaking phase with the stripe ferromagnetic order have different symmetries, there must exist two additional phase transition points between these two SPT phases and symmetry breaking phase. The detailed analysis of the phase diagram is given in the Appendix A.

B. Wave functions for \mathbb{Z}_2 topologically ordered phases

Since the \mathbb{Z}_2 topologically ordered states can be obtained by gauging the \mathbb{Z}_2 SPT states²⁸, we construct the tensor networks for \mathbb{Z}_2 topologically ordered states based on the previous \mathbb{Z}_2 SPT tensor network states. At first we promote the global \mathbb{Z}_2 symmetry to \mathbb{Z}_2 gauge symmetry by introducing the \mathbb{Z}_2 gauge fields on two adjacent plaquettes, see in Fig.4(b), and the original \mathbb{Z}_2 spins are coupled to the \mathbb{Z}_2 gauge fields. Then integrating out the physical degrees of freedom gives rise to the tensor network wave functions for the \mathbb{Z}_2 topologically ordered phases. After the gauging procedure, the trivial \mathbb{Z}_2 SPT state becomes the toric code state, while the non-trivial SPT state is related to the double semion state²⁸.

When the \mathbb{Z}_2 gauge fields are introduced with the local tensor \mathcal{D} :

$$\mathcal{D}_{l'r'r'}^{i_e} = D_{l'r}^{i_e} \delta_{l'r'}^{i_e}, \quad (10)$$

where $D_{10}^1 = D_{01}^1 = D_{00}^0 = D_{11}^0 = 1$, otherwise $D_{l'r}^{i_e} = 0$. The physical degrees of freedom i_e located at the edges

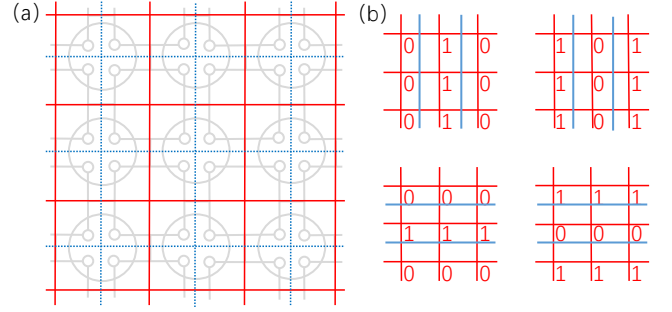


FIG. 3: (a) If the inter-site plaquette (gray square) is grouped as a single spin at the vertices of the red lattice, the tensor network wave functions can be further simplified, and the original lattice sites form the blue square lattice. (b) On the red lattice, those four symmetry breaking ground states for the tensor network state $|\psi\rangle$ are displayed, the numbers attached to the vertices of the red lattice are the values of the \mathbb{Z}_2 spins, and the ground states have the stripe-like ferromagnetic long-range order. The symmetry breaking ground state configurations for $|\Psi\rangle$ are denoted by the blue lines, which are the domain walls of spin configurations.

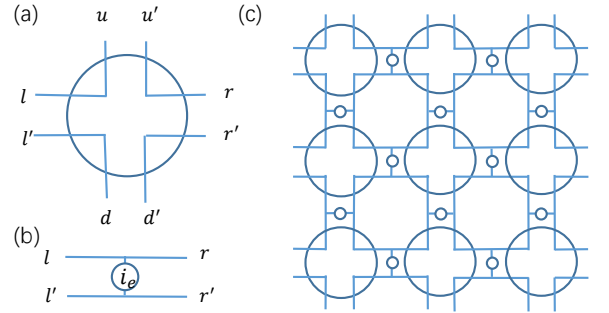


FIG. 4: (a) The local tensor \mathcal{A} on the vertices of the lattice. (b) The local tensor \mathcal{D} on the edges of the lattice. (c) The tensor network wave function for the \mathbb{Z}_2 topologically ordered phases.

of the lattice are \mathbb{Z}_2 gauge field, and other indices stand for the virtual degrees of freedom. The local tensor \mathcal{D} actually detects the existence of the domain walls between the adjacent inter-site plaquettes, as shown in Fig.4(c). Including the tensor \mathcal{D} into the original SPT tensor network states leads to the gauged SPT tensor network wave function:

$$|\Psi'\rangle = \sum_{\{i_e\}\{s_\alpha\}} \text{tTr}(\tilde{\mathcal{A}} \otimes \mathcal{D} \cdots \otimes \tilde{\mathcal{A}} \otimes \mathcal{D}) |i_1 i_2 \cdots\rangle |s_1 s_2 \cdots\rangle. \quad (11)$$

Then we can integrate out all \mathbb{Z}_2 spins by performing the overlap $\prod \sum_{s_\alpha s_\beta s_\gamma s_\delta} \langle s_\alpha s_\beta s_\gamma s_\delta | \Psi'\rangle$, where the bra state is the equal weight superposition of all spin configurations and the product runs over all the lattice sites. And the

tensor network wave function for topologically ordered phases with only \mathbb{Z}_2 gauge fields is thus obtained:¹⁰

$$|\Psi(\lambda)\rangle = \sum_{\{i_e\}} \text{tTr}(\mathcal{A} \otimes \mathcal{D} \cdots \otimes \mathcal{A} \otimes \mathcal{D}) |i_1 i_2 i_3 \cdots\rangle, \quad (12)$$

where the local tensor \mathcal{A} is given by

$$\mathcal{A}_{ll'rr'uu'dd'} = A^{lu'r'd} \delta_{ul} \delta_{u'r'} \delta_{r'd'} \delta_{l'd}, \quad (13)$$

displayed in Fig. 4, and the local tensor A has been defined by Eq. (8). Compared to the original local tensor $\tilde{\mathcal{A}}$, \mathcal{A} does not include any physical indices.

Since almost all data of topological order are encoded in the modular matrices which are determined by properties of MPOs, we can verify that the tensor network wave function $|\Psi(\lambda = 1)\rangle$ yields the fixed-point tensor network state of the toric code model, while $|\Psi(\lambda = -1)\rangle$ yields the fixed point tensor network state of the double semion model. The detail analysis are given in the Appendix B. Unlike the unitary transformation W for the SPT states, the unitary transformation exchanging $|\Psi(\lambda)\rangle$ and $|\Psi(-\lambda)\rangle$ becomes non-local in the sense that it can not be expressed as a product of local operators. However, this non-local unitary transformation plays the similar role as the duality transformation from the toric code phase to the double semion phase, so $\lambda = 0$ is also the self-dual point, describing the quantum topological phase transition between two topologically ordered phases.

Similarly the wave function $|\Psi(\lambda)\rangle$ for $|\lambda| \gg 1$ also corresponds to the symmetry breaking phase with two degenerate ground states: one consists of all vertical domain walls and the other consists of all horizontal domain walls, as shown in Fig. 3(b). Because two spin configurations correspond to one domain wall configuration, the ground-state degeneracy of the symmetry breaking phase is less than four. Two topological phases with topological orders are significantly distinct from the symmetry breaking phase, we can expect the presence of two additional phase transition points separating the two topologically ordered phases from the symmetry breaking phase in the full parameter space.

In addition, as shown in Fig. 5, the MPOs for the respective SPT phases now become the MPOs for the corresponding topologically ordered phases, because the local tensors \mathcal{A} and \mathcal{D} are invariant under the action of the the respective MPO. For the topologically ordered phases, it has been known that the ground state degeneracy on a torus is four, and these four degenerate wavefunctions correspond to the present tensor network wave function without the MPO insertion, and with the MPO insertion in either horizontal or vertical direction, or in both directions, respectively. Moreover, the properties of these MPOs can also give rise to the modular matrices for these two intrinsically \mathbb{Z}_2 topological phases, which is crucial for identifying the characteristics of topological order. The detail is also presented in the Appendix B.

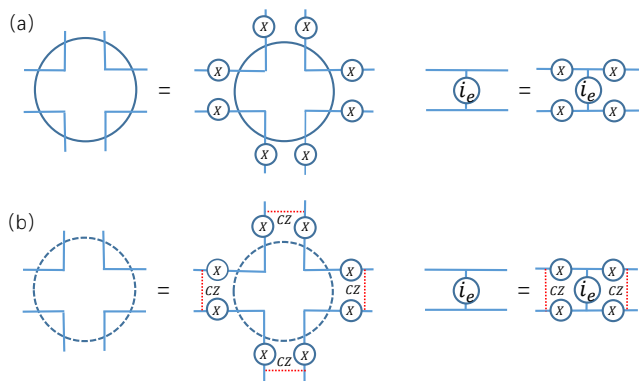


FIG. 5: The gauge symmetry of the local tensors of the topological states. (a) For the toric code state, the local tensors \mathcal{A} and \mathcal{D} are invariant under the MPO action of U_x . (b) For the double semion state, the local tensors are invariant under the MPO action the gauge symmetry of U_{czx} .

III. QUANTUM TRANSFER OPERATORS AND COMPLETE PHASE DIAGRAM

A. Quantum transfer operators

Since the \mathbb{Z}_2 SPT states and the \mathbb{Z}_2 topologically ordered states are associated by the gauging procedure, which preserves the energy gap of the parent Hamiltonians of the tensor network states¹⁶, we will expect that the structure of the phase diagram for the topologically ordered states is similar to that for the SPT states¹⁷. The complete phase diagram of the general tensor-network with topological order can be mapped out by calculating the correlation length as a function of λ .

In the tensor network representation, the correlation length can be extracted from the dominant eigenvalues of the one-dimensional quantum transfer operator \mathbb{T} , while the transfer operator is defined by the tensor network wave function norm on a torus,

$$\langle \Psi | \Psi \rangle = \text{Tr}(\mathbb{T}^{N_x}), \quad (14)$$

which is a double layer tensor network obtained by contracting the physical indices of the tensor network (ket layer) and its complex conjugate (bra layer), as displayed in Fig. 6(a). The one-dimensional quantum transfer operator is the repeating unit of the double tensor network. Here N_x is the number of lattice sites in the x direction and the circumference of the transfer operator is given by N_y in Fig. 6(b). N_x can be a very large number while N_y is limited by the numerical calculations.

In general, all kinds static correlation functions are closely related the quantum transfer operator \mathbb{T} (Ref.²⁹). Since its eigenvalue spectrum contains essential information about the bulk properties of systems^{18,29}, such a one-dimensional quantum transfer operator can be viewed as a matrix with the left indices as the row and right indices as the column so that the numerical calculations can be performed. The transfer operator is usually not

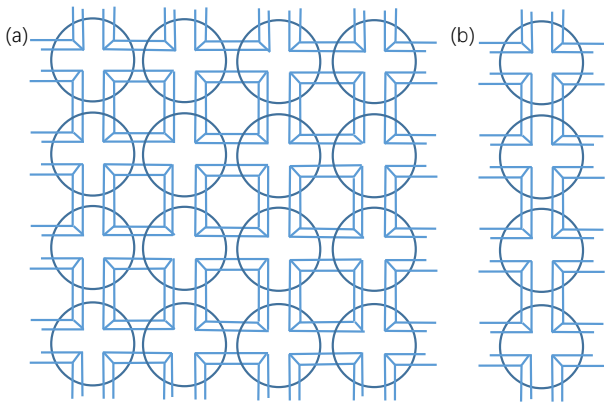


FIG. 6: (a) The double layer tensor network of wavefunction norm $\langle \Psi | \Psi \rangle$, where the left and right, up and down indices should be contracted periodically. (b) The one-dimensional quantum transfer operator, where the up and down indices should be connected periodically.

necessarily hermitian, but we can take the modulus of the eigenvalues. The finite degeneracy of the dominant eigenvalues indicates the presence of either topological order or long-range order with a spontaneous symmetry breaking. Therefore, the one-dimensional quantum transfer operator plays the essential role in the present tensor network state approach. It is the central object which we study in this paper.

The quantum transfer operator generally includes the bra and ket layer structures. For the topological phases, the spin degrees of freedom in the bra layer and the ket layer are connected by the same domain wall degrees of freedom, so the spin configurations in both bra and ket layers are either the same or opposite. Then the transfer operator can be decomposed into

$$\mathbb{T} = \mathbb{T}_0 \oplus \mathbb{T}_1, \quad (15)$$

where \mathbb{T}_0 is one subblock with the same spin configurations in the bra and ket layers and \mathbb{T}_1 is the second subblock with the opposite spin configurations in the bra and ket layers. Actually the transfer operator also inherits the MPO symmetry of the local tensors, which includes two \mathbb{Z}_2 symmetries acting on the bra and ket layers respectively:

$$\mathbb{Z}_2 \otimes \mathbb{Z}_2 = \{\mathbb{1} \otimes \mathbb{1}, \mathbb{1} \otimes U_\phi, U_\phi \otimes \mathbb{1}, U_\phi \otimes U_\phi\}, \quad (16)$$

where ϕ is ‘x’ for $\lambda > 0$ and ‘czx’ for $\lambda < 0$, and

$$U_x = \prod_j X_j^{\otimes 2}, \quad U_{czx} = \prod_j X_j^{\otimes 2} \prod_j CZ_{j,j+1}, \quad (17)$$

with $X_j^{\otimes 2}$ acts on the j -th half plaquette and $CZ_{j,j+1}$ acts on the j -th and $(j+1)$ -th half plaquettes.

Since two subblocks \mathbb{T}_0 and \mathbb{T}_1 can be changed into each other by the transformations $\mathbb{1} \otimes U_\phi$ or $U_\phi \otimes \mathbb{1}$, the eigenvalue spectra of \mathbb{T}_0 and \mathbb{T}_1 are the same. However, the eigenstates of \mathbb{T} break the symmetry $\mathbb{1} \otimes U_\phi$ and $U_\phi \otimes \mathbb{1}$

but preserve the symmetry $U_\phi \otimes U_\phi$, so the $\mathbb{Z}_2 \otimes \mathbb{Z}_2$ symmetry is broken down to \mathbb{Z}_2 , leading to the exact two-fold degeneracy of the topological phases. It has been established that different symmetry breaking patterns in the virtual degrees of freedom of the transfer operator correspond to the phases with distinct topological orders, so this kind of symmetry breaking pattern just corresponds to the intrinsically \mathbb{Z}_2 topological phases^{18–21}.

As the unitary transformation exchanging the wave functions $|\Psi(\lambda)\rangle$ and $|\Psi(-\lambda)\rangle$ acts on the physical degrees of freedom, the transfer operators of $\mathbb{T}(\lambda)$ and $\mathbb{T}(-\lambda)$ are also related to each other by the unitary transformation acting on the virtual degrees of freedom. Specially, the unitary transformation acting on the subspace in which the degrees of freedom in the bra and ket layers are opposite is given by $U_{cz} \otimes \mathbb{1}$ or $\mathbb{1} \otimes U_{cz}$, where $U_{cz} = \prod_j CZ_{j,j+1}$. Then the eigenvalue spectra of $\mathbb{T}(\lambda)$ and $\mathbb{T}(-\lambda)$ are the same and symmetric about the self-dual point $\lambda = 0$, implying that the resulting transfer operator spectra for both toric code phase and double semion phase are the same. As for the differences between these two topological phases, we will discuss them in the following sections, while the self-dual point $\lambda = 0$ is very intricate, where there is an emergent MPO symmetry U_{cz} .

B. Transfer operators with flux insertions

For the topologically ordered phases, the ground states are degenerate on a manifold with non-trivial topology. In the tensor network formalism, these degenerate ground states can be related by the MPO insertion in different directions. Thus, the complete transfer operators should include the transfer operator with different MPO insertions. For the topological phases, the MPO operator U_ϕ can be inserted in the bra or ket layer of the double layer tensor network, and the resulted transfer operator is denoted as \mathbb{T}^ϕ or \mathbb{T}_ϕ . However, such transfer operators are not meaningful because they represent vanished overlaps between different ground states. So we must insert the MPO operator U_ϕ in both layers of the tensor networks, the resulting transfer operator is denoted as \mathbb{T}_ϕ^ϕ and shown in Figs.7(a) and (b). Inserting such a MPO flux into the transfer operator is equivalent to the insertion of the MPO flux into \mathbb{T}_0 and \mathbb{T}_1 separately. So the operators \mathbb{T}_ϕ^ϕ can be further expressed as

$$\mathbb{T}_\phi^\phi = \mathbb{T}_{0,\phi}^\phi \oplus \mathbb{T}_{1,\phi}^\phi. \quad (18)$$

Similarly the transfer operator \mathbb{T}_ϕ^ϕ also exhibits the $\mathbb{Z}_2 \times \mathbb{Z}_2$ symmetry. But the eigenstates of \mathbb{T}_ϕ^ϕ break the $\mathbb{Z}_2 \times \mathbb{Z}_2$ symmetry down to \mathbb{Z}_2 in the virtual degrees of freedom, signifying the \mathbb{Z}_2 topological order with a two-fold degeneracy in the eigenvalue spectrum. Meanwhile, the transfer operator $\mathbb{T}_\phi^\phi(\lambda)$ is also related to $\mathbb{T}_\phi^\phi(-\lambda)$ by the unitary transformation, and their eigenvalue spectra

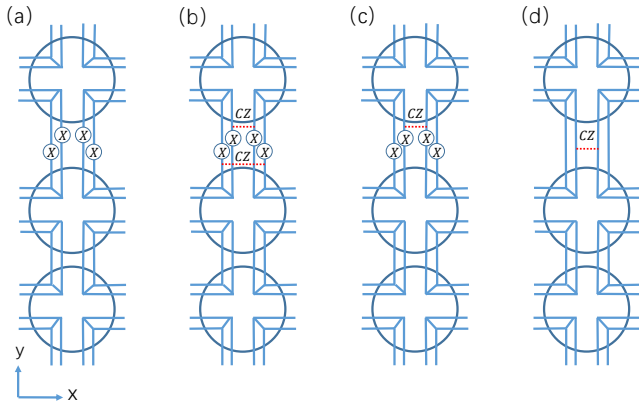


FIG. 7: The flux inserted transfer operators \mathbb{T}_x^x , \mathbb{T}_{czx}^{czx} , \mathbb{T}_{czx}^x , and \mathbb{T}_{cz} are shown in (a), (b), (c) and (d), respectively.

are the same and symmetric about $\lambda = 0$. So we just need to calculate the eigenvalue spectrum of $\mathbb{T}_x^x(\lambda)$ with $\lambda > 0$ in the following discussion.

By the way, we would like to point out that the transfer operators for the intrinsically \mathbb{Z}_2 topological phases have a close relationship with those transfer operators for the SPT phases. \mathbb{T}_0 is the transfer operator of the tensor networks for the SPT phases, while $\mathbb{T}_{0,\phi}^\phi$ corresponds to the transfer operator of the SPT tensor network with the extrinsic symmetric defect, which has been used to detect the non-trivial SPT property^{16,30–33}.

C. Transfer operators at $\lambda = 0$

Different from the tensor network states for the finite values of λ , the tensor network state at $\lambda = 0$ has both MPO symmetries U_{czx} and U_x , because the topological properties for both sides of the topologically ordered phases are inherited. Notice that MPOs of U_x and U_{czx} do not commute, so the gauge symmetry for the tensor network state is not the simple $\mathbb{Z}_2 \times \mathbb{Z}_2$ symmetry. Since there are two different MPO symmetries, we can insert different MPOs in the bra and ket layers of the tensor networks, e.g., \mathbb{T}_{czx}^x shown in Fig.7(c). Actually, the MPOs of U_x and U_{czx} in the same layer can be fused into a new MPO of U_{cz} when there is no MPO insertion in the other direction. Then such a new MPO as the unitary transformation $\mathbb{1} \otimes U_{cz}$ becomes an emergent symmetry of the transfer operator. Inserting this new MPO in one of the bra and ket layers of the double layer tensor networks gives rise to the twisted transfer operator \mathbb{T}_{cz} , see Fig. 7(d). Although there are other possible ways of inserting MPOs, they turn out to be either a vanished transfer operator or the transfer operator whose spectrum is equivalent to \mathbb{T} , \mathbb{T}_x^x , \mathbb{T}_{czx}^x and \mathbb{T}_{cz} , respectively.

D. Complete phase diagram

The correlation length of the general tensor network state wave function $|\Psi(\lambda)\rangle$ can be calculated from the diagonalizing the complete transfer operator $\mathbb{T} \oplus \mathbb{T}_\phi^\phi$ with the largest circumference of the transfer operators $N_y = 20$ in the numerical calculations. Each eigenvalue of \mathbb{T} and \mathbb{T}_ϕ^ϕ should have a two-fold degeneracy at least. In Fig.8(a), we display the numerical results of the quantities $-1/\ln|\frac{d_i}{d_1}|$, where d_i is the i -th largest eigenvalue of the transfer operator $\mathbb{T} \oplus \mathbb{T}_\phi^\phi$. In the topological phases, the correlation length is determined by $\xi = -1/\ln|\frac{d_5}{d_1}|$, because the largest eigenvalue has four-fold degeneracy in the topological phases. In the symmetry breaking phase, however, $\xi = -1/\ln|\frac{d_9}{d_1}|$, due to the presence of an eight-fold degeneracy. For $|\lambda| \gg 1$, the present tensor network description contains a redundancy in the symmetry breaking phase: one domain wall configuration corresponds to two spin configurations.

According to the divergence of the correlation lengths shown in Fig. 8(a), we can thus identify three different QCPs at $\lambda = 0$ and $\lambda = \pm 1.73$, dividing the phase diagram into three different gapped phases: the toric code phase ($0 < \lambda < 1.73$), the double semion phase ($-1.73 < \lambda < 0$), and the symmetry breaking phase ($|\lambda| > 1.73$). The fixed point tensor network states of the toric code and double semion models locate at $\lambda = \pm 1$ and have zero correlation length.

In Fig. 8(b), the correlation length in the different lattice sizes satisfies $\xi \propto N_y$ at the phase transition point $\lambda = 0$, indicating that the correlation length tends to infinite in the thermodynamic limit. So the topological phase transition is continuous and the transition point is a QCP. In Fig. 8(e), the critical exponent of the correlation length is determined as $\nu = \nu' \simeq 1.60$ for both $\lambda \rightarrow 0^-$ and $\lambda \rightarrow 0^+$. At $|\lambda_c| \approx 1.73$, however, the correlation length is defined by $\xi = -1/\ln|\frac{d_5}{d_1}|$ for $|\lambda| < 1.73$, and $-1/\ln(|\frac{d_9}{d_1}|)$ for $|\lambda| > 1.73$, which are found to be proportional to the circumference of the transfer operator N_y as shown in Figs.8 (c) and (d), respectively. Thus these two phase transition points at $\lambda = \pm 1.73$ are also QCPs. In Figs. 8 (f) and (g), the critical exponents of the correlation length on both sides of the transition point are fitted as $\nu \simeq 0.78$ for $|\lambda| \rightarrow 1.73^-$ and $\nu' \simeq 0.77$ for $|\lambda| \rightarrow 1.73^+$, which are almost the same value. Since the critical exponent at $\lambda = 0$ is almost twice larger than that at the critical point $|\lambda| = 1.73$, the former correlation length looks less divergent than the latter. Therefore, the full phase diagram is displayed in Fig. 8(h), where the arrows indicate the decreasing direction of the correlation length, consistent with the renormalization group flow.

To reveal the mechanism of the quantum topological phase transitions, the transfer operator spectra are separated into different topological sectors and the useful information can be extracted from dominant eigenvalues

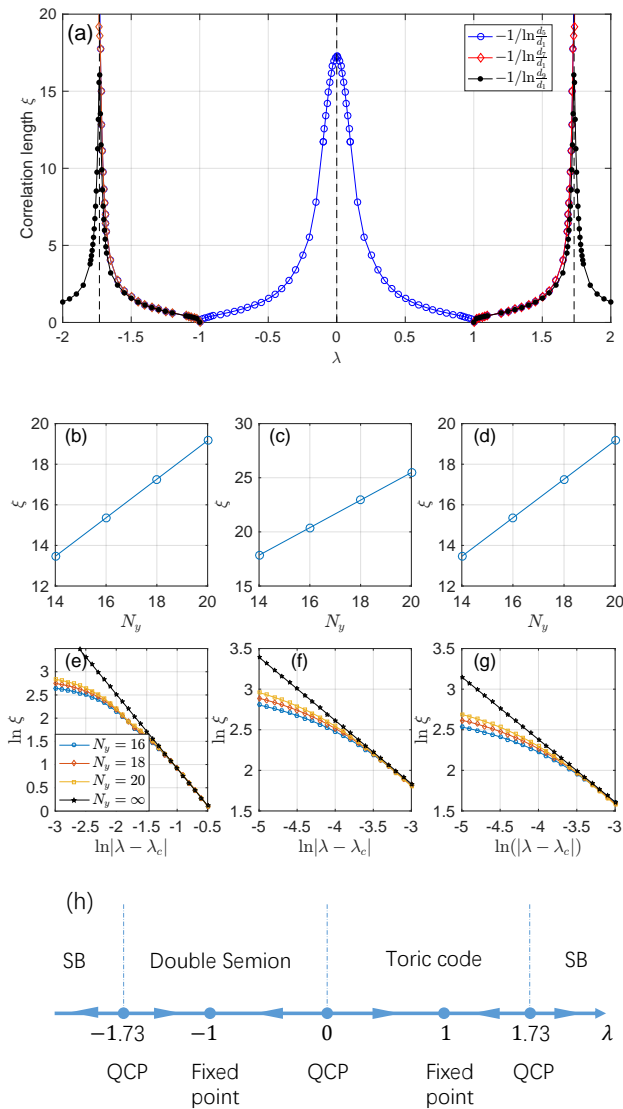


FIG. 8: (a) The quantities $-1/\ln|\frac{d_i}{d_1}|$ as functions of λ , where d_i is the i -th dominant eigenvalue of the transfer operator $\mathbb{T} \oplus \mathbb{T}_x^x$. Here the circumference of the transfer operator is chosen as 18 sites. (b), (c), (d) The finite correlation length satisfies $\xi \propto N_y$ at $\lambda = 0$, $\lambda \approx 1.73^-$, and $\lambda \approx 1.73^+$, respectively. (e),(f),(g) The critical exponent ν of the correlation length is fitted at $\lambda \rightarrow 0$, $|\lambda| \rightarrow 1.73^-$ and $|\lambda| \rightarrow 1.73^+$. (h) The phase diagram is plotted and several special points are marked, where the arrows denote the decreasing direction of the correlation length as a function of the parameter λ .

belonging to each topological sectors. Since both \mathbb{T} and \mathbb{T}_ϕ^ϕ commute with $U_\phi \otimes U_\phi$, their eigenstates carry the \mathbb{Z}_2 charges of $U_\phi \otimes U_\phi$. According to the \mathbb{Z}_2 charges, the eigenvalues can be divided into four sectors, corresponding to four types of anyons of \mathbb{Z}_2 topological order^{18,34}. In Fig.9, we display the dominant eigenvalues of the transfer operator $\mathbb{T} \oplus \mathbb{T}_\phi^\phi$ in the different topological sectors as a function of λ . In the vicinity of $\lambda \simeq 1.73$, the dominant eigenvalues of four topological sectors become de-

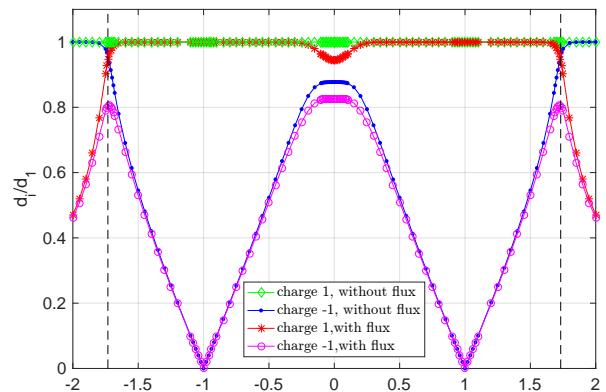


FIG. 9: The dominant eigenvalues of four different sectors of the transfer operator. ‘Charge 1’ and ‘charge -1’ are \mathbb{Z}_2 charge of $U_\phi \otimes U_\phi$. ‘With flux’ or ‘without flux’ denotes the eigenvalues obtained from \mathbb{T} or \mathbb{T}_ϕ^ϕ .

generate in the thermodynamical limit as λ is varied to approach the symmetry breaking phase. In the symmetry breaking phase, the sectors with the same flux and different charges are degenerate, suggesting that the full $\mathbb{Z}_2 \times \mathbb{Z}_2$ symmetry of the transfer operator is broken and the bosonic charge condensation occurs. On the other hand, the dominant eigenvalues of the sectors with the flux insertion are apparently smaller than those of sectors without flux, signifying the flux excitations must be confined into pairs^{18,19,21}.

As we expected, the dominant eigenvalues in the vicinity at $\lambda = -1.73$ show the same behavior as that at $\lambda = 1.73$. However, the topological sectors have different interpretations. The anyons in the toric code phase and double semion phase have the one-to-one correspondence: the electric charge \mathbf{e} corresponds to the semion-antisemion pair \mathbf{b} ; the flux \mathbf{m} corresponds to the semion \mathbf{s} , and the fermion \mathbf{f} correspond to anti-semion $\bar{\mathbf{s}}$. Therefore, the phase transition at $\lambda = -1.73$ can also be interpreted as the condensation of \mathbf{b} with the semion \mathbf{s} and anti-semion $\bar{\mathbf{s}}$ confinement. Nevertheless, the phase transition at $\lambda = 0$ does not belong to such anyon condensation picture.

IV. MAPPING TO CLASSICAL STATISTICAL MODELS

It is known that a class of two-dimensional quantum systems with their many-body ground state wave functions can be mapped to the partition functions of the classical statistical systems, because their ground state wave functions can be written in terms of the Boltzmann weights^{8,22,23,35-37}. In order to explore the topological phase transitions in the above phase diagram, we would like to derive the corresponding classical statistical models of the quantum wave functions with \mathbb{Z}_2 topological order.

To map onto a classical statistical model, we have to

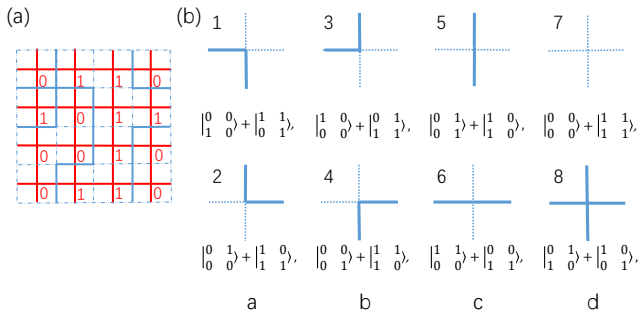


FIG. 10: (a) Each spin configuration on the red lattice (and its opposite configuration) is associated to a domain wall configuration on the blue lattice. (b) The \mathbb{Z}_2 symmetric superpositions of the intra-site spin types have the one-to-one correspondence to the eight-vertex types, where a , b , c and d are the Boltzmann weights of the vertex types in each column, separately. The number of each vertex type is shown in the upper left corner.

implement the local tensor contractions of the tensor network wave functions. Notice that the virtual degrees of freedom of the tensor network states are \mathbb{Z}_2 spins, and their physical degrees of freedom are the domain walls. Two spin configurations correspond to one domain wall configuration, one of them is shown in Fig. 10(a). A correspondence of the spin types of the intra-site plaquette and domain wall types of a vertex on the blue lattice can be figured out, displayed in Fig.10(b). Since the domain wall configurations of the quantum wave functions can be built by the eight different kinds of domain walls on the vertices of the blue lattice, the configurations of the quantum ground states are as the same as the configurations of the classical eight-vertex model (up to a transformation on one of the sublattices). There are four states $|0011\rangle$, $|1001\rangle$, $|0110\rangle$ and $|1100\rangle$ of the intra-site plaquettes weighted by λ , which correspond to the 5-th and 6-th domain wall types on a vertex, so the general tensor network wave functions can be expressed as

$$\begin{aligned}
 |\Psi(\lambda < 0)\rangle &= \sum_{\{i_e\}} \lambda^{n_5+n_6} \prod w(s_\alpha s_\beta s_\gamma s_\delta) |i_1 i_2 i_3 \dots\rangle, \\
 |\Psi(\lambda > 0)\rangle &= \sum_{\{i_e\}} \lambda^{n_5+n_6} |i_1 i_2 i_3 \dots\rangle,
 \end{aligned} \tag{19}$$

where n_j is the total number of the j -type vertices in the closed domain wall configuration, $w(s_\alpha s_\beta s_\gamma s_\delta)$ has been defined in Sec. II, and the product runs over all the intra-site plaquettes of the configurations $\{s_\alpha s_\beta s_\gamma s_\delta\}$ that the configurations $\{i_e\}$ correspond to. Although one domain wall configuration corresponds to the two spin configurations, the quantity $\prod w(s_\alpha s_\beta s_\gamma s_\delta)$ is the same for the two spin configurations.

In the eight-vertex model³⁸, the Boltzmann weights of vertex types in the each column of Fig.10(b) are denoted by a , b , c and d , and the corresponding partition function

of the eight-vertex model is given by

$$\mathcal{Z} = \sum_{\{i_e\}} a^{n_1+n_2} b^{n_3+n_4} c^{n_5+n_6} d^{n_7+n_8}. \tag{20}$$

The quantum-classical correspondence is usually given by identifying the norm of the many-body wave function with the partition function:

$$\mathcal{Z} = \langle \Psi(\lambda) | \Psi(\lambda) \rangle = \sum_{\{i_e\}} \lambda^{2(n_5+n_6)}. \tag{21}$$

Compare to Eq. (20), we immediately notice the Boltzmann weights

$$a = b = d = 1, \quad c = \lambda^2, \tag{22}$$

which indicate that the phases in the range $\lambda < 0$ of the phase diagram is equivalent to the phases in the range $\lambda > 0$. Namely, from the viewpoint of the statistical models, both double semion and toric code phases belong to the same paramagnetic disordered phase. Furthermore, it is well-established that the eight-vertex model becomes critical under the condition³⁸: $c = a + b + d$. From the exact solutions of the eight-vertex model, the exact positions of the QCPs should be at $\lambda = \sqrt{3}$, which are perfectly consistent with our numerical results. In the limit of $c = 0$, the eight-vertex model is reduced to the critical six-vertex model, corresponding to the QCP at $\lambda = 0$.

Moreover, it has been known that the effective field theory of the critical eight-vertex model is described by the two-dimensional Euclidean massless free boson CFT compactified on a circle with a radius²²

$$R^2 = \frac{4}{\pi} \operatorname{arccot}(\sqrt{cd}), \quad \text{for } c = d + 2, \tag{23}$$

which gives rise to $R = \sqrt{2/3}$. Because the free boson CFT with the compactified radii R and $2/R$ are dual to each other³⁹, the the *dual* CFT should have $R = \sqrt{6}$. The critical exponents of the correlation length at $\lambda = \sqrt{3}$ are thus known as $\nu = \nu' = 3/4$, which are also close to our numerical values.

Although the exact phase transition points can be acquired by mapping the quantum wave functions to the classical statistical models, the nontrivial sign factor $\prod w(s_\alpha s_\beta s_\gamma s_\delta)$ in the wave functions $|\Psi(\lambda < 0)\rangle$ has completely vanished. In other words, the distinct topological nature between the tensor network states $|\Psi(\lambda < 0)\rangle$ and $|\Psi(\lambda > 0)\rangle$ vanishes, and both the double semion and toric code wave functions are mapped to the same classical eight-vertex model. In this sense, the quantum-classical mapping has *not* kept all the important information on the quantum many-body phases, so the quantum topological phase transition between two distinct topologically ordered phases at $\lambda = 0$ can not be understood from the critical six-vertex model. More importantly, the ground states of a topologically ordered

phase have a degeneracy on a torus, and different ground states can be related by inserting the MPOs into the tensor network states, which is not included in the quantum-classical mapping as well. So we have to decode the critical properties of the QCPs by employing other methods in the tensor network approach.

V. CONFORMAL QUANTUM CRITICALITIES

A. Central charges

Although the phase transitions from the topological phases to the symmetry breaking phase can be explained by anyon condensation^{19,21}, the quantum phase transition between two topological phases is still mysterious. Meanwhile only a few attempts have considered the phase transitions between the toric code and double semion models^{19,21,40}. In this section, we will study the QCPs from the full spectra of the transfer operators without/with the flux insertions, and the underlying field theories of the QCPs can be revealed.

It has been demonstrated that the spectrum of the transfer operator defined from the wave function norm contains much useful information of the bulk properties of the tensor network states^{18,29}. We have used the dominant eigenvalues of the transfer operator to deduce the correlation length. The previous numerical correlation length shows that $\xi \propto N_y$ at three QCPs, so we can further calculate the entanglement entropy from the corresponding dominant eigenvector of the transfer operator \mathbb{T} . After the numerical entanglement entropy is obtained, we can fit the numerical results with the Calabrese-Cardy formula⁴¹,

$$S(n, N_y) = \frac{c}{3} \ln \left[\frac{N_y}{\pi} \sin \left(\frac{\pi n}{N_y} \right) \right] + \text{const.}, \quad (24)$$

where n is the segment length chosen in the bipartition of the dominant eigenvector with a given circumference N_y , and the central charge c for the QCPs are extracted and shown in Fig.11(a) and (b). The fitting central charge is estimated as $c \approx 1$ for both $\lambda = 0$ and $\lambda = \pm\sqrt{3}$, indicating that the quantum criticalities of all these three QCPs are characterized by a two-dimensional compactified free boson CFT!

It has been argued that the moduli of eigenvalues of the transfer operator correspond to the minimum of the excitation spectrum of the bulk system²⁹, and the one-dimensional quantum transfer operator is a manifestation of the holographic bulk-boundary correspondence⁹. Instead of solving the model Hamiltonians in two dimension, it is more efficient to extract the properties of low-energy excitations from the transfer operator spectra. When the quantities $\epsilon_i = -\ln \left| \frac{d_i}{d_1} \right|$ defined from the eigenvalues of the transfer operators are carefully analyzed, we surprisingly find that the finite-size scaling law $\epsilon_i \propto \frac{1}{N_y}$ exactly satisfies at the critical points, suggest-

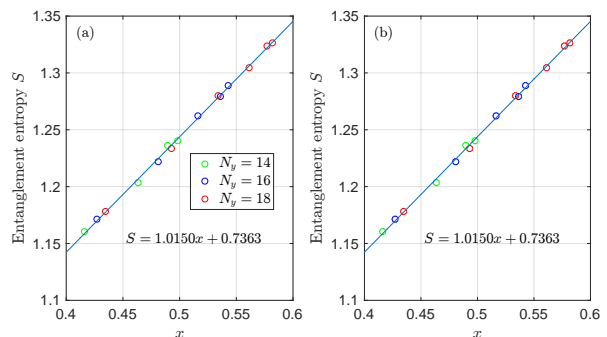


FIG. 11: (a) The entanglement entropy is calculated from the dominant eigenstate of the transfer operator $\mathbb{T}(\lambda = 0)$ and fitted with the Calabrese-Cardy formula to extract the central charge. Here $x(n, N_y) = \frac{1}{3} \ln \left[\frac{N_y}{\pi} \sin \left(\frac{\pi n}{N_y} \right) \right]$ and n is the lattice site number of the subsystem in the bipartition. (b) The similar analysis for the transfer operator $\mathbb{T}(\lambda = \pm\sqrt{3})$.

ing that ϵ_i can be regarded as the spectral levels of the finite-size spectrum of the corresponding CFTs.

B. Finite-size spectra at $\lambda = \sqrt{3}$

The finite-size spectrum ϵ_i at $\lambda = \sqrt{3}$ can be a function of the lattice momentum, which is extracted from the translation symmetry. Since the transfer operator $\mathbb{T} \oplus \mathbb{T}_\phi^\phi$ has the MPO symmetry of $U_\phi \otimes U_\phi$, the eigenstates of this transfer operator can be decomposed into two different sectors by the \mathbb{Z}_2 charges of $U_\phi \otimes U_\phi$. Moreover, the transfer operator \mathbb{T} has the translation symmetry $T \otimes T$, where T separately acts on the bra and ket layers and shifts the j -th half plaquette to the $(j-1)$ -th half plaquette. Although the transfer operator \mathbb{T}_ϕ^ϕ breaks the translation symmetry, a modified translation symmetry^{30,31,33} can be found as $\tilde{T} = TX_j X_{j+1}$ for $\lambda > 0$ and $\tilde{T} = TCZ_{j,j+1} X_j X_{j+1}$ for $\lambda < 0$, where the flux is inserted on the j -th half plaquettes, see Fig. 7(a), and the modified translation operators acts on the j -th and $(j+1)$ -th plaquettes.

However, the eigenvalue spectra ϵ_i of \mathbb{T} and \mathbb{T}_ϕ^ϕ do not yield the complete CFT spectra directly. The complete CFT spectrum includes both the \mathbb{Z}_2 charge 1 and -1 sectors of the operator $\mathbb{T} \oplus \mathbb{T}_\phi^\phi$. Figs.12(a) and (b) show the finite-size spectra ϵ_i with respect to the momenta, and the spectral levels are rescaled such that the ϵ_i can be fitted to the scaling dimensions of the primary fields of the compactified free boson CFT:

$$\Delta(e, m) = \frac{e^2}{R^2} + \frac{m^2 R^2}{4}, \quad (25)$$

where e denotes the total angular momenta of the primary fields, m is the winding numbers of the primary fields, $s = em$ are the conformal spins of primary fields³⁹,

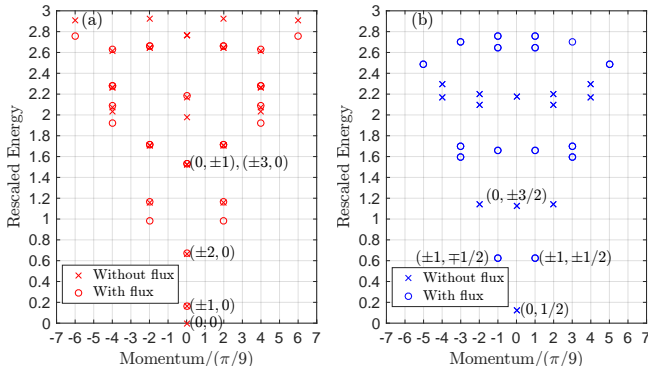


FIG. 12: (a) The spectrum of the charge 1 sector of the transfer operator $\mathbb{T} \oplus \mathbb{T}_\phi^\pm$ at $\lambda = \sqrt{3}$. (b) The corresponding charge -1 sector. Here the momentum is calculated from the squared translation operator T_l^2 or \tilde{T}_l^2 with $N_y = 18$ lattice sites and the spectral levels are rescaled such that they can perfectly match the scaling dimensions. The red and blue signs marks the ± 1 charges of the symmetry $U_\phi \otimes U_\phi$. The cross and circle markers the levels from \mathbb{T} or \mathbb{T}_ϕ^\pm . The scaling dimensions of the primary fields are denoted by (e, m) .

and the compactified radius has been found as $R = \sqrt{6}$. Both quantum numbers of e and m are normally chosen as integers in the charge 1 sector, corresponding to the CFT spectrum of the critical eight-vertex model. From the scaling dimensions $\Delta = h + \bar{h}$ and conformal spins $s = h - \bar{h}$, we can determine the primary fields with the conformal dimensions (h, \bar{h}) , see the Table I. The reason why the sector with the charge 1 corresponds to the finite-size spectrum of the eight-vertex model is that this sector corresponds to the ground-state wave function in which the domain walls are closed. It is also known that the compactified free boson CFT with $R = \sqrt{k}$ is denoted as the $U(1)_k$ CFT⁴², and the charge 1 sector thus belongs to the $U(1)_6$ CFT.

TABLE I: Primary fields, scaling dimensions, and conformal spins of the charge 1 sector for the QCP at $\lambda = \sqrt{3}$.

Primary fields (h, \bar{h})	Scaling dimensions (e, m)	Scaling dimensions $\Delta = h + \bar{h}$	Conformal spins $s = h - \bar{h}$
(0, 0)	(0, 0)	0	0
(3/4, 3/4)	(0, ± 1)	3/2	0
(1, 0)	/	1	1
(0, 1)	/	1	-1
(1/3, 1/3)	($\pm 2, 0$)	2/3	0
(1/12, 1/12)	($\pm 1, 0$)	1/6	0

However, in the charge -1 sector, the conformal dimensions of primary fields are independent of R and are fixed as 1/16 and 9/16 (Ref.⁴³), so the scaling dimensions can be expressed as $\Delta(e, m) = \frac{e^2}{2} + \frac{m^2}{2}$. The primary fields, scaling dimensions and their conformal spins are given in Table II. Moreover, the momenta of spectral levels are determined as $\frac{2\pi}{N_y}(\mathbb{Z} + \frac{1}{2})$, representing the topo-

logical anyon excitations. Therefore, the quantum criticality of this QCP exhibits two different characteristics: the spontaneous symmetry breaking and confinement of the topological anyon excitations.

TABLE II: Primary fields, scaling dimensions, and conformal spins of the charge -1 sector for the QCP at $\lambda = \sqrt{3}$.

Primary fields (h, \bar{h})	Scaling dimensions (e, m)	Scaling dimensions $\Delta = h + \bar{h}$	Conformal spins $s = h - \bar{h}$
(1/16, 1/16)	(0, $\pm 1/2$)	1/8	0
(1/16, 9/16)	($\pm 1, \mp 1/2$)	5/8	-1/2
(9/16, 1/16)	($\pm 1, \pm 1/2$)	5/8	1/2
(9/16, 9/16)	(0, $\pm 3/2$)	9/8	0

Actually the combination of the charge 1 and charge -1 sectors can be interpreted as the \mathbb{Z}_2 orbifold $U(1)_6$ free boson CFT with the compactified radius $R = \sqrt{6}$. Fig. 12(a) corresponds to the spectrum of the untwisted sector, while Fig. 12(b) represents the spectrum of the twisted sector^{43,44}. Since the \mathbb{Z}_2 orbifold CFT characterizes the critical properties of the Ashkin-Teller model, the present QCP belongs to the universality class of the Ashkin-Teller model at the \mathbb{Z}_4 parafermion point^{43,45}.

C. Finite-size spectra at $\lambda = -\sqrt{3}$

As we discussed in the previous section, the QCP at $\lambda = -\sqrt{3}$ is similar to the QCP at $\lambda = \sqrt{3}$, and the spectra of the transfer operators are as the same as Fig. 12. So the QCP also belongs to the universality class of the Ashkin-Teller model at the \mathbb{Z}_4 parafermion point, and the quantum phase transition is caused by the boson condensation and semion/anti-semion confinement. Therefore, just from the transfer operator spectra, we can not make the distinction between the QCP at $\lambda = -\sqrt{3}$ and the QCP at $\lambda = \sqrt{3}$. However, in the entanglement spectrum of the double semion phase, we have known that the semion and anti-semion sectors should carry quarter-integer momenta $\frac{2\pi}{N_y}(n \pm \frac{1}{4})$ with $n \in \mathbb{Z}$. Then it is expected that the spectral levels of the transfer operators in the topological sectors with charge -1 should also carry quarter integer momenta in the double semion phase. Nevertheless, the eigenvalues of the lattice translational operator T are given by $\frac{2\pi}{N_y}(n \pm \frac{1}{4})$, and thus the eigenvalues of $T \otimes T$ are obtained as either $\frac{2\pi}{N_y}(n + \frac{1}{2})$ or $\frac{2\pi}{N_y}n$. Unlike the toric code phase, the spectral momenta (conformal spins) in the semion and anti-semion sectors are not properly associated to the topological spins. Distinguishing these two critical points can be seen in the wave functions of the toric code phase and double semion phase. The essential difference just exists in the quasi-particle braiding statistics, which can be obtained from the modular matrices. So it is reasonable that we can not distinguish them via the transfer operator spectra and

the corresponding static correlators. We have resolved this problem by investigating the dominant eigenvectors of the transfer operators and some arguments are provided in Appendix C.

D. Finite-size spectra at $\lambda = 0$

The QCP at $\lambda = 0$ is very exotic, describing the continuous topological phase transition between two topologically ordered phases. Essentially different from the QCPs at $\lambda = \pm\sqrt{3}$, it is more natural to classify the finite-size spectra of the transfer operators at $\lambda = 0$ according to the absence or presence of the flux insertion. As we discussed in Sec.III, we can have four different transfer operators: \mathbb{T} , \mathbb{T}_{cz} , \mathbb{T}_x^x , and \mathbb{T}_{czz}^x , leading to topologically different sectors. The corresponding eigenstates of \mathbb{T}_x^x , \mathbb{T}_{czz}^x and \mathbb{T}_{cz} carry the symmetry charges of $U_x \otimes U_x$, $U_x \otimes U_{czz}$ and $\mathbb{1} \otimes U_{cz}$, respectively. Since \mathbb{T} commutes with $U_x \otimes U_x$, $U_{cz} \otimes U_{cz}$ and $U_{czz} \otimes U_{czz}$ and the eigenstates preserve these symmetries, we can use the quantum numbers associated with these symmetries to label the spectral levels.

Moreover, the insertion of MPOs breaks the translation symmetry $T \otimes T$, so we need to use the modified translational operators^{30,31,33}. For \mathbb{T}_x^x , the modified translation symmetry is expressed as $(TX_j X_{j+1}) \otimes (TX_j X_{j+1})$, where the MPOs are inserted on the plaquettes of the j -th row and the operators act on the vicinity edges of the j and $(j+1)$ -th half plaquette. The modified translational symmetry for \mathbb{T}_{cz} is given by $T \otimes (TCZ_{j,j+1})$, while the modified translational operator for \mathbb{T}_{czz}^x is $(TX_j X_{j+1}) \otimes (TCZ_{j,j+1} X_j X_{j+1})$.

In Fig. 13(a), the spectrum of \mathbb{T} is displayed, and the spectral levels are labelled by the quantum numbers of the translation symmetry $T \otimes T$ and \mathbb{Z}_2 charge of $U_x \otimes U_x$. By carefully fitting the spectra with the scaling dimensions $\Delta(e, m) = \frac{e^2}{R^2} + \frac{m^2 R^2}{4}$, we found that the full spectrum can be described by the $U(1)$ compactified free boson CFT with a compactified radius $R \approx \sqrt{8/3}$. The conformal dimensions of primary fields for such a theory are determined by

$$h = \left(\frac{e}{R} + \frac{mR}{2} \right)^2, \quad \bar{h} = \left(\frac{e}{R} - \frac{mR}{2} \right)^2. \quad (26)$$

Moreover, the symmetry charge of the $U_x \otimes U_x$ carried by the spectral levels satisfies the rule $(-1)^e$, and the fields in the same conformal tower have the identical \mathbb{Z}_2 charge. Fig. 13(b) is also the spectrum of \mathbb{T} but the spectral levels are labelled by the \mathbb{Z}_2 charge of the symmetry $\mathbb{1} \otimes U_{cz}$, which is determined by the rule $(-1)^m$. When the spectrum of \mathbb{T} is further labelled by the charge of the symmetry $U_x \otimes U_{czz}$ in Fig. 13(c), the low-energy fields satisfy the rule $(-1)^{e+m}$, similar to the entanglement spectrum of the \mathbb{Z}_2 nontrivial SPT phase^{26,31,32}. These features are summarized in the first two columns of Table. III.

TABLE III: Symmetry of MPO, symmetry charges of \mathbb{T} , \mathbb{T}_x^x , \mathbb{T}_{cz} and \mathbb{T}_{czz}^x , and fractionalization of e and m for the QCP at $\lambda = 0$. The first two columns show properties of \mathbb{T} , the last four columns display properties of \mathbb{T}_x^x , \mathbb{T}_{cz} and \mathbb{T}_{czz}^x .

Symmetry of \mathbb{T}	Symmetry charges of \mathbb{T}	After S transform	e	m	Symmetry charges
$U_x \otimes U_x$	$(-1)^e$	\mathbb{T}_x^x	\mathbb{Z}	$\mathbb{Z} + \frac{1}{2}$	$(-1)^e$
$\mathbb{1} \otimes U_{cz}$	$(-1)^m$	\mathbb{T}_{cz}	$\mathbb{Z} + \frac{1}{2}$	\mathbb{Z}	$(-1)^m$
$U_x \otimes U_{czz}$	$(-1)^{e+m}$	\mathbb{T}_{czz}^x	$\mathbb{Z} + \frac{1}{2}$	$\mathbb{Z} + \frac{1}{2}$	$-i(-1)^{e+m}$

Furthermore, we can also calculate the finite-size spectra of the transfer operators with the flux insertions, describing the topological excitations with fractionalized quantum numbers. The resulting spectra are also well-fitted into the $U(1)$ compactified free boson CFT with the compactified radius $R = \sqrt{8/3}$, and can be divided into three sets of spectra. Fig. 14(a) shows the first set of spectra from the operator \mathbb{T}_x^x with the \mathbb{Z}_2 charge of $U_x \otimes U_x$, and the winding numbers m are determined as half-integers and the angular momenta of boson fields e as integers. The \mathbb{Z}_2 charges are given by $(-1)^e$, the levels in the same conformal tower have the identical \mathbb{Z}_2 charge, but the momenta of the spectral levels with the charge -1 are half-integers $\frac{2\pi}{9}(\mathbb{Z} + \frac{1}{2})$. The second set of spectra from the operator \mathbb{T}_{cz} is displayed in Fig. 14(b), where the eigenstates of \mathbb{T}_{cz} carry the charge of $\mathbb{1} \otimes U_{cz}$ and the scaling dimensions of the primary fields are given by the integer m and half-integers e . But the symmetry charges are determined by $(-1)^m$, and the levels with the charge -1 also carry half-integer momenta. Fig. 14(c) shows the third set of spectra from the operator \mathbb{T}_{czz}^x , where the eigenstates carry the charges of $U_x \otimes U_{czz}$ and both the quantum numbers m and e are half-integers. However, it should be emphasized that the eigenvalues of $U_x \otimes U_{czz}$ are $\pm i$, which are determined by $-i(-1)^{e+m}$, so that the spectral levels carry the *quarter*-integers momenta $\frac{2\pi}{9}(\mathbb{Z} \pm \frac{1}{4})$. Such a compactified free boson CFT has been predicted for the entanglement spectrum of the \mathbb{Z}_2 nontrivial SPT phases with symmetry defects^{30-33,46}. These results are displayed in the last four columns of Table. III. All these three sets of CFT spectra reflect the rich structure of the low-energy excitations at the QCP.

Actually there are close relations between the above two types of spectra. Considering the fact that the actions of symmetries $U_x \otimes U_x$, $\mathbb{1} \otimes U_x$ and $U_x \otimes U_{czz}$ on the low-energy excitations are given by $(-1)^e$, $(-1)^m$ and $-i(-1)^{e+m}$, respectively, we can analytically derive the corresponding the partition function of compactified boson CFT modular after the modular S transformation using the Poisson resummation^{32,39,42}. Then the quantum numbers of e and m are fractionalized into half-integers in different way according to the symmetry actions for the three cases, as shown in each row of Table. III. These results coincide with our numerical spectra. Thus, the three sets of excitations in Fig.13 and those three sets in Fig.14 have an exact one-to-one mapping through the

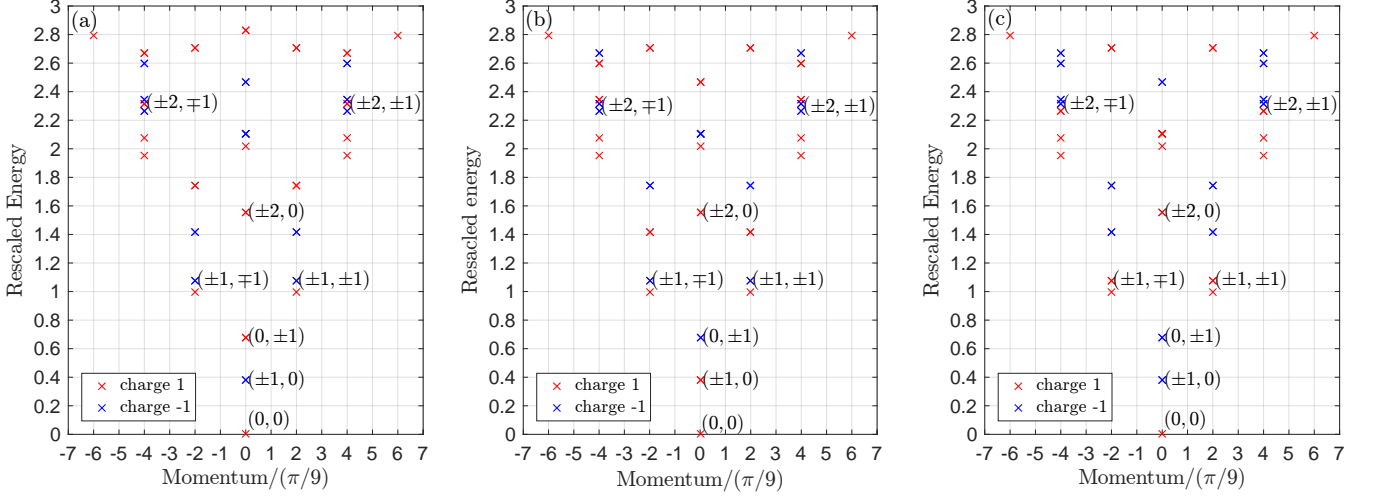


FIG. 13: The spectra of the transfer operator \mathbb{T} for the QCP at $\lambda = 0$, where the spectral levels are labelled by \mathbb{Z}_2 symmetry charge of $U_x \otimes U_x$ in (a), the \mathbb{Z}_2 symmetry charge of $\mathbb{1} \otimes U_{cz}$ in (b), and the \mathbb{Z}_2 symmetry charge of $U_x \otimes U_{czz}$ in (c). Here the transfer operators include $N_y = 18$ lattice sites and the spectral levels are rescaled such that they perfectly match the scaling dimensions. The red and blue signs denote the \mathbb{Z}_2 charge ± 1 of the corresponding symmetry. The primary fields are expressed by (e, m) .

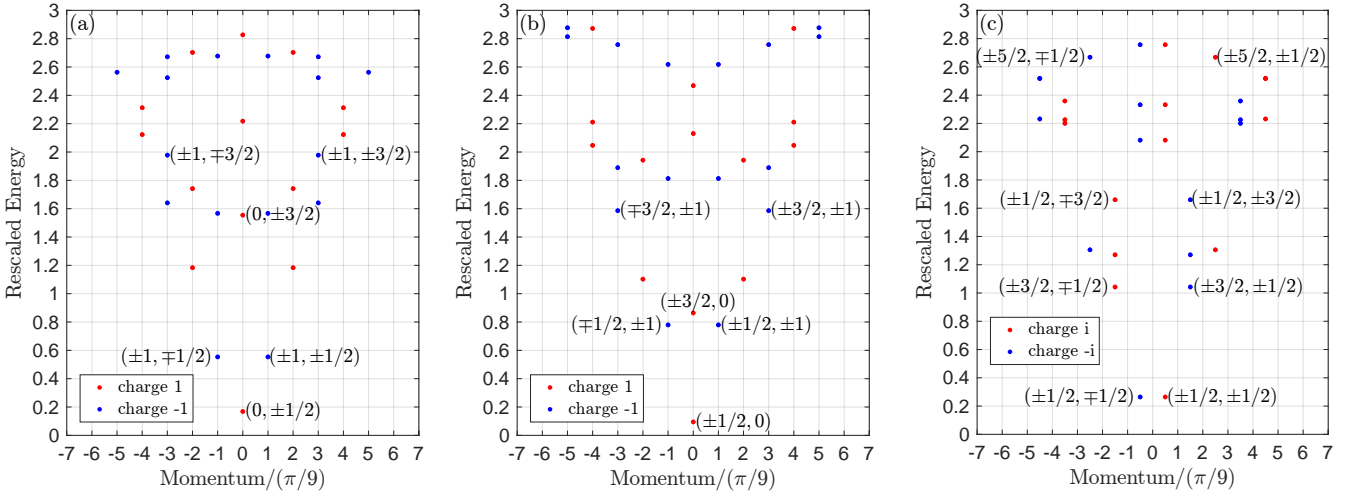


FIG. 14: The spectra of the transfer operators with the flux insertions. (a) \mathbb{T}_x^x , (b) \mathbb{T}_{cz} and (c) \mathbb{T}_{czz}^x . The red and blue dots stand for the \mathbb{Z}_2 charges ± 1 of the corresponding symmetry. Here the transfer operators include $N_y = 18$ lattice sites and the momentum is calculated from the square of the modified translation operator and the energy levels are rescaled such that they perfectly match the scaling dimensions of the primary fields (e, m) .

modular S transformation.

VI. DISCUSSION AND CONCLUSION

It is intuitively expected that the quantum criticalities of a two-dimensional quantum system should be described by (2+1)-dimensional CFTs. However, in our tensor network state approach, the quantum topological phase transitions of the two-dimensional quantum system are related to (2+0)-dimensional time-independent

CFTs in the sense that the ground state static correction functions of 2-dimensional quantum systems are equal to the correlators of (2+0)-dimensional CFTs. How to understand such numerical results?

In the literature, there exist two different scenarios to approach the quantum topological phase transitions⁴⁷. In the first ‘‘Hamiltonian deformation’’ approach, where two distinct fixed-point model Hamiltonians are interpolated with a parameter, a QCP may reach at a critical value of the parameter and the corresponding effective action has the Lorentz invariance with the dynamical

critical exponent $z = 1$, and the QCP is thus described by a (2+1)-dimensional CFT. In the second approach, however, the QCP sits on the different path called “wave function deformation” in the parameter space, where the effective action is not Lorentz-invariant, characterized by the dynamical critical exponent $z > 1$ due to the intrinsic space-time asymmetry. In addition, the corresponding tensor network states with *algebraically* decaying correlation functions keep a finite bond dimension even at the critical point⁴⁸. So a phenomenon of holographic dimensionality reduction occurs, and the essential information about the low-energy excitations has been encoded in the one-dimensional quantum transfer operators without/with the flux insertions. Such QCPs belong to the so-called Rokhsar-Kivelson type⁴⁹ conformal QCPs²², because the action is invariant under conformal transformation of two-dimensional space.

Although the static correlation functions at these QCPs are characterized by the compactified free boson CFT, the dynamics of these QCPs can be different, depending on the dynamic symmetry class²³. Because there is an $U(1)$ symmetry along the critical line, the quantum six-vertex model obeys the scaling with a dynamical exponent $z = 2$. So the QCP at $\lambda = 0$ should belong to the quantum Lifshitz theory²². However, the QCPs at $\lambda = \pm\sqrt{3}$ are more difficult to have a concrete conclusion, as the quantum eight-vertex model possesses dynamical exponent $z \geq 2$ in their critical regime, it was suggested that such conformal QCPs may not be the final stabilized fixed points under the renormalization group transformation and they may flow to the stable (2+1)-dimensional Lorentz-invariant QCPs with $z = 1$ relativistic dynamics in the end^{22,23}. On the other hand, up to one-loop approximation, a recent renormalization group study around this critical point has shown that the dynamical exponent does not flow⁵⁰ in contrast to the previous classical Monte Carlo study²³. Thus, further investigations are certainly needed to clarify this issue.

More importantly, the QCPs at $\lambda = \pm\sqrt{3}$ have two different aspects. They represent a quantum phase transition from the quantum symmetric phase to the symmetry breaking phase, corresponding to the conventional disorder-order phase transition of the eight-vertex model. On the other hand, they also characterize a quantum topological phase transition from the topologically ordered (anyon deconfined) phase to the topologically trivial (anyon confined) phase, which can be explained by the mechanism of anyon condensation. However, the QCP at $\lambda = 0$ *can not* be understood within such a mechanism, because the quantum phase transition occurs at the end point of disordered phase of the classical statistical model. The corresponding criticality contains a rich CFT structure of low-energy topological excitations.

To summarize, we have proposed the tensor network state approach to the quantum topological phase transitions and their criticalities in two dimensions. By gauging a tensor network state of \mathbb{Z}_2 SPT phases with a tuning parameter λ , we have constructed a general tensor net-

work state wave function for the intrinsically \mathbb{Z}_2 topological phases, which incorporates the toric code phase, double semion phase, and the symmetry breaking phase. From the calculation of the correlation length defined from the one-dimensional quantum transfer operator, we have mapped out the full phase diagram and identified three QCPs at $\lambda = \pm\sqrt{3}$ and $\lambda = 0$, respectively. Then we have further proved that the quantum criticalities at these three QCPs can be extracted from the complete spectra of the transfer operators without/with the flux insertions. The static correlators of resulting conformal QCPs should be described by the (2+0)-dimensional time-independent $U(1)$ compactified free boson CFTs. There are many open questions, e.g, how to expand the present tensor network approach to the topological phase transitions among \mathbb{Z}_3 topologically ordered phases? In addition, the conformal QCPs for the topological phase transitions of the non-abelian topological phases are also interesting. These issues are left for future works.

Acknowledgment.- The authors would like to thank Guo-Yi Zhu for his stimulating discussions and acknowledges the support of National Key Research and Development Program of China (2017YFA0302902).

Appendix A: Phase diagram for \mathbb{Z}_2 SPT phases

As we mentioned before, the transfer operator for SPT states is \mathbb{T}_0 , so we can calculate the ground state phase diagram from it. For larger λ , the numerical calculation shows that the dominant eigenvalues of the transfer operator have nearly four-fold degeneracy, because the splitting between these nearly degenerate eigenvalues becomes exponentially small when increasing the system size. This observation is consistent with the previous analysis that the spontaneous symmetry breaking occurs for larger $|\lambda|$. While for smaller $|\lambda|$, the dominant eigenvalue is non-degenerate.

In the range that the dominant eigenvalue is four-fold degenerate, the finite-size correlation length is defined by $\xi = -1/\ln(|\frac{d_5}{d_1}|)$, where d_i is the i -th dominant eigenvalues, while it is $\xi = -1/\ln(|\frac{d_2}{d_1}|)$ in the range that the dominant eigenvalue is non-degenerate. The calculated correlation length ξ is displayed in Fig.15 for $|\lambda| \in [0, 2]$. There exists three special points $\lambda_c = 0$ and $\lambda_c = \pm 1.73$. At $\lambda_c = 0$, the finite-size scaling of correlation length in Fig.15(b) leads to $\xi \propto N_y$, where N_y is the circumference of the transfer operator \mathbb{T}_0 . So the correlation length is divergent in the thermodynamic limit, corresponding to a QCP. By carefully fitting the critical exponent of the correlation length in the vicinity critical point with $\xi \sim |\lambda|^{-\nu}$, we can extract the critical exponent $\nu \simeq 1.62$ shown in Fig.15(e). Since the correlation length is symmetric about $\lambda = 0$, the critical exponent for both sides is the same.

However, close to $|\lambda_c| \simeq 1.73$, the finite-size correlation length is defined by $\xi = -1/\ln(\frac{d_2}{d_1})$ for $|\lambda| < 1.73$,

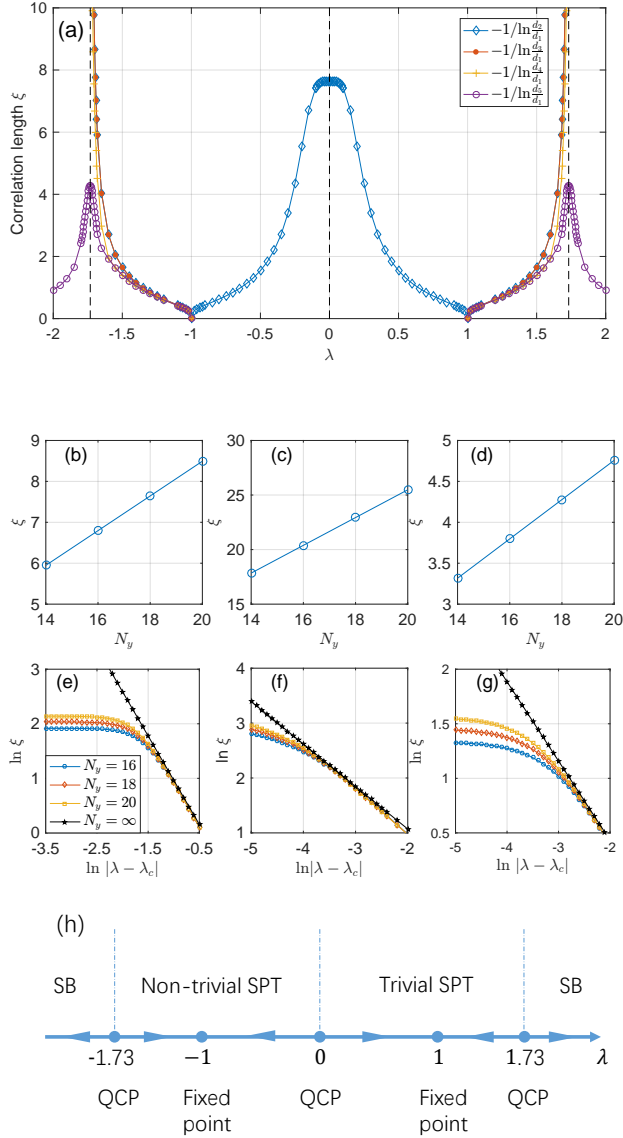


FIG. 15: (a) The quantities $-1/\ln \frac{d_i}{d_1}$ of the SPT wave function as function of λ , where d_i is the i -th dominant eigenvalue of \mathbb{T}_0 and the circumference of the transfer operator is $N_y = 18$. (b), (c), (d) The correlation length $\xi \propto N_y$ at $\lambda = 0$, around $|\lambda| = 1.73^-$, and $|\lambda| = 1.73^+$, respectively. (e),(f),(g) The critical exponent μ of ξ at $\lambda \rightarrow 0$, $\lambda \rightarrow 1.73^-$, and $\lambda \rightarrow 1.73^+$, respectively. (h) The phase diagram is plotted and several special points are marked, where the arrows denote the decreasing direction of the correlation length.

while it is $\xi = -1/\ln(\frac{d_5}{d_1})$ for $|\lambda| > 1.73$. Fig.15 (c) and (d) indicate that the corresponding numerical values are proportional to N_y . Therefore, $\lambda \approx \pm 1.73$ correspond to two different QCPs and the critical exponents of the correlation length for $|\lambda| \rightarrow 1.73^-$ and $|\lambda| \rightarrow 1.73^+$ can also be determined as $\nu = 0.77$ and $\nu' = 0.73$, as shown in Fig.15 (f) and (g). At $\lambda = \pm 1$, the correlation length $\xi = 0$ corresponds to the stabilized fixed points of the SPT phases.

Appendix B: Modular matrices of topologically ordered phases

The wave functions of topological states are given in Eq. (19). Although the fixed point wave function of the double semion model is different from the Levin-Gu wave function²⁸, it can be demonstrated that, using the MPOs and modular matrices, it is indeed the double semion state.

For topological states, the ground states have four-fold degeneracy on torus, corresponding to the tensor network states without MPO inserting, with MPO inserting in the horizontal direction, with MPO inserting in the vertical direction, and with MPO inserting in both directions. The resulted wave functions are $|\Psi(\mathbb{1}, \mathbb{1})\rangle$, $|\Psi(\mathbb{1}, U_\phi)\rangle$, $|\Psi(U_\phi, \mathbb{1})\rangle$ and $|\Psi(U_\phi, U_\phi)\rangle$, where the winding numbers of domain walls of $|\Psi(\mathbb{1}, \mathbb{1})\rangle$ in the two directions are both even, and inserting MPO changes the winding number parities of the corresponding directions from even to odd. Notice that these wave functions are not the minimally entangled states⁷, but are their linear combinations.

In general, the only differences between the toric code and double semion phases are the braiding statistics of anyons, which is encoded in the modular matrices. There are two modular matrices: S encodes the mutual braiding statistics of anyons and T encodes the self-braiding statistics. Under the basis consisting of the wave functions $|\Psi(\mathbb{1}, \mathbb{1})\rangle$, $|\Psi(\mathbb{1}, U_\phi)\rangle$, $|\Psi(U_\phi, \mathbb{1})\rangle$ and $|\Psi(U_\phi, U_\phi)\rangle$, the modular matrices of the toric code model can be calculated as¹⁷

$$S = \begin{pmatrix} 1 & 0 & 0 & 0 \\ 0 & 0 & 1 & 0 \\ 0 & 1 & 0 & 0 \\ 0 & 0 & 0 & 1 \end{pmatrix}, T = \begin{pmatrix} 1 & 0 & 0 & 0 \\ 0 & 1 & 0 & 0 \\ 0 & 0 & 0 & 1 \\ 0 & 0 & 1 & 0 \end{pmatrix}, \quad (\text{B1})$$

and those for the double semion model are

$$S = \begin{pmatrix} 1 & 0 & 0 & 0 \\ 0 & 0 & 1 & 0 \\ 0 & 1 & 0 & 0 \\ 0 & 0 & 0 & -1 \end{pmatrix}, T = \begin{pmatrix} 1 & 0 & 0 & 0 \\ 0 & 1 & 0 & 0 \\ 0 & 0 & 0 & -1 \\ 0 & 0 & 1 & 0 \end{pmatrix}. \quad (\text{B2})$$

The sign difference in S and T of the toric code model and double semion model can be derived from the properties of MPOs. When there exists a MPO in one direction for the double semion model, the combination of two MPOs or the inverse the MPO in the other direction will give rise to a minus sign⁵¹, as shown in Fig.16. This is resulted by the fact that the operators $CZ_{j,j+1}$ and $X_j X_{j+1}$ do not commute, i.e., $CZ_{j,j+1} X_j X_{j+1} = -X_j X_{j+1} CZ_{j,j+1} Z_j Z_{j+1}$. However, one can easily verify that $\prod_i X_i^{\otimes 2}$ and $\prod_i CZ_{i,i+1}$ commute when acting on the periodic plaquettes and anti-commute when acting on the twisted plaquettes (inserting a symmetry twist $X_i X_{i+1}$ in another direction), as shown in Fig.16. The minus sign in $-Z_i Z_{i+1}$ is cancelled because we the considered systems have even number of sites in both directions.

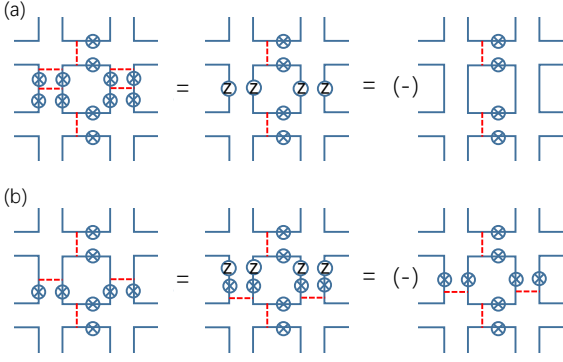


FIG. 16: (a) Composing two MPOs in the x direction in the presence of a MPO in the y direction induces a minus sign in the S matrix, where X and Z denote the Pauli matrices and the red dash lines are CZ gates. (b) Inverting the MPO in the x direction in the presence of a MPO in the y direction also gives rise to a minus sign in the T matrix.

Appendix C: Momenta related to topological spins

A possible way to determine the momenta related to of the eigenstates is the momentum polarization⁵². But the momentum polarization for a single site translation is not well-defined for the non-chiral topological states, so we can only consider the well-defined translation of $2N_y$ sites (4π rotation)³⁰, and calculate the momentum polarization for the translation of $2N_y$ sites and properly determine the anyon sectors. As we mentioned in the Sec.III, the double layer transfer operator is $\mathbb{T} = \mathbb{T}_0 \oplus \mathbb{T}_1$, where \mathbb{T} has the $\mathbb{Z}_2 \times \mathbb{Z}_2$ symmetry. Assuming that the dominant eigenstate of \mathbb{T}_0 is σ and that of \mathbb{T}_1 is σ' and considering the $U_{czz} \otimes \mathbb{1}$ symmetry is broken, we then have

$$\sigma = U_{czz}\sigma'\mathbb{1}, \sigma' = U_{czz}\sigma\mathbb{1}. \quad (\text{C1})$$

The similar arguments hold for \mathbb{T}_{czz}^{czz} and

$$\sigma_{czz} = -U_{czz}\sigma'_{czz}\mathbb{1}, \sigma'_{czz} = U_{czz}\sigma_{czz}\mathbb{1}, \quad (\text{C2})$$

where σ_{czz} and σ'_{czz} are the dominant eigenstates of $\mathbb{T}_{0,czz}^{czz}$ and $\mathbb{T}_{1,czz}^{czz}$. Although the dominant eigenstates of \mathbb{T} and \mathbb{T}_{czz}^{czz} break the symmetries $\mathbb{1} \otimes U_{czz}$ and $U_{czz} \otimes \mathbb{1}$, we can restore these symmetries by linearly combining the dominant eigenstates³⁴, because the reduced density matrix can be linear combinations of σ , σ' , σ_{czz} and σ'_{czz} . So we have the symmetric dominant eigenstates

$$\begin{aligned} \rho &= \sigma + \sigma', \rho' = \sigma - \sigma' \\ \rho_{czz} &= \sigma_{czz} + i\sigma'_{czz}, \rho'_{czz} = \sigma_{czz} - i\sigma'_{czz}, \end{aligned} \quad (\text{C3})$$

which satisfies

$$\begin{aligned} U_{czz}\rho\mathbb{1} &= \rho, U_{czz}\rho'\mathbb{1} = -\rho', \\ U_{czz}\rho_{czz}\mathbb{1} &= -i\rho_{czz}, U_{czz}\rho'_{czz}\mathbb{1} = i\rho'_{czz}. \end{aligned} \quad (\text{C4})$$

By considering the constraints

$$T^{2N_y} = \mathbb{1}, \tilde{T}^{2N_y} = U_{czz}^2, \quad (\text{C5})$$

the momentum polarizations with $2N_y$ site translation are thus given by

$$\begin{aligned} \text{tr}(\mathbb{1}\rho) &= 1, \text{tr}(\mathbb{1}\rho') = 1, \\ \text{tr}(U_{czz}^2\rho_{czz}) &= -1, \text{tr}(U_{czz}^2\rho'_{czz}) = -1, \end{aligned} \quad (\text{C6})$$

which means that the 4π rotation acquires a minus sign for the sectors with flux and the topological spins are $\pm i$. Therefore, the momenta of excitations in the semion and anti-semion sectors should have a correction.

¹ A. Y. Kitaev, Annals of Physics **303**, 2 (2003), ISSN 0003-4916, URL <http://www.sciencedirect.com/science/article/pii/S0003491602000180>.

² A. Kitaev, Annals of Physics **321**, 2 (2006), ISSN 0003-4916, URL <http://www.sciencedirect.com/science/article/pii/S0003491605002381>.

³ M. A. Levin and X.-G. Wen, Physical Review B **71** (2005), ISSN 1098-0121, 1550-235X, URL <https://link.aps.org/doi/10.1103/PhysRevB.71.045110>.

⁴ Z.-C. Gu, M. Levin, B. Swingle, and X.-G. Wen, Physical Review B **79** (2009), ISSN 1098-0121, 1550-235X, URL <https://link.aps.org/doi/10.1103/PhysRevB.79.085118>.

⁵ X.-G. Wen, Rev. Mod. Phys. **89**, 041004 (2017), URL <https://link.aps.org/doi/10.1103/RevModPhys.89.041004>.

⁶ F. A. Bais and J. K. Slingerland, Phys. Rev. B **79**, 045316 (2009), URL <https://link.aps.org/doi/10.1103/PhysRevB.79.045316>.

1103/PhysRevB.79.045316.

⁷ Y. Zhang, T. Grover, A. Turner, M. Oshikawa, and A. Vishwanath, Phys. Rev. B **85**, 235151 (2012), URL <https://link.aps.org/doi/10.1103/PhysRevB.85.235151>.

⁸ F. Verstraete, M. M. Wolf, D. Perez-Garcia, and J. I. Cirac, Phys. Rev. Lett. **96**, 220601 (2006), URL <https://link.aps.org/doi/10.1103/PhysRevLett.96.220601>.

⁹ J. I. Cirac, D. Poilblanc, N. Schuch, and F. Verstraete, Phys. Rev. B **83**, 245134 (2011), URL <https://link.aps.org/doi/10.1103/PhysRevB.83.245134>.

¹⁰ H. He, H. Moradi, and X.-G. Wen, Phys. Rev. B **90**, 205114 (2014), URL <https://link.aps.org/doi/10.1103/PhysRevB.90.205114>.

¹¹ W.-J. Rao, X. Wan, and G.-M. Zhang, Phys. Rev. B **90**, 075151 (2014), URL <https://link.aps.org/doi/10.1103/PhysRevB.90.075151>.

¹² W.-J. Rao, G.-M. Zhang, and K. Yang, Phys. Rev. B

- 93, 115125 (2016), URL <https://link.aps.org/doi/10.1103/PhysRevB.93.115125>.
- ¹³ W.-J. Rao, G.-Y. Zhu, and G.-M. Zhang, Phys. Rev. B **93**, 165135 (2016), URL <https://link.aps.org/doi/10.1103/PhysRevB.93.165135>.
- ¹⁴ Z.-Q. Wang, G.-Y. Zhu, and G.-M. Zhang, ArXiv e-prints (2018), 1802.04542.
- ¹⁵ N. Bultinck, M. Mariën, D. J. Williamson, M. B. Şahinoğlu, J. Haegeman, and F. Verstraete, Annals of Physics **378**, 183 (2017), ISSN 0003-4916, URL <http://www.sciencedirect.com/science/article/pii/S0003491617300040>.
- ¹⁶ D. J. Williamson, N. Bultinck, M. Mariën, M. B. Şahinoğlu, J. Haegeman, and F. Verstraete, Phys. Rev. B **94**, 205150 (2016), URL <https://link.aps.org/doi/10.1103/PhysRevB.94.205150>.
- ¹⁷ C.-Y. Huang and T.-C. Wei, Phys. Rev. B **93**, 155163 (2016), URL <https://link.aps.org/doi/10.1103/PhysRevB.93.155163>.
- ¹⁸ J. Haegeman, V. Zauner, N. Schuch, and F. Verstraete, NATURE COMMUNICATIONS **6**, 8 (2015), ISSN 2041-1723, URL <http://dx.doi.org/10.1038/ncomms9284>.
- ¹⁹ K. Duivenvoorden, M. Iqbal, J. Haegeman, F. Verstraete, and N. Schuch, Phys. Rev. B **95**, 235119 (2017), URL <https://link.aps.org/doi/10.1103/PhysRevB.95.235119>.
- ²⁰ M. Mariën, J. Haegeman, P. Fendley, and F. Verstraete, Phys. Rev. B **96**, 155127 (2017), URL <https://link.aps.org/doi/10.1103/PhysRevB.96.155127>.
- ²¹ M. Iqbal, K. Duivenvoorden, and N. Schuch, Phys. Rev. B **97**, 195124 (2018), URL <https://link.aps.org/doi/10.1103/PhysRevB.97.195124>.
- ²² E. Ardonne, P. Fendley, and E. Fradkin, Annals of Physics **310**, 493 (2004), ISSN 00034916, URL <http://linkinghub.elsevier.com/retrieve/pii/S0003491604000247>.
- ²³ S. V. Isakov, P. Fendley, A. W. W. Ludwig, S. Trebst, and M. Troyer, Phys. Rev. B **83**, 125114 (2011), URL <https://link.aps.org/doi/10.1103/PhysRevB.83.125114>.
- ²⁴ X. Chen, Z.-C. Gu, Z.-X. Liu, and X.-G. Wen, Phys. Rev. B **87**, 155114 (2013), URL <https://link.aps.org/doi/10.1103/PhysRevB.87.155114>.
- ²⁵ X. Chen, Z.-X. Liu, and X.-G. Wen, Phys. Rev. B **84**, 235141 (2011), URL <https://link.aps.org/doi/10.1103/PhysRevB.84.235141>.
- ²⁶ X. Chen and X.-G. Wen, Phys. Rev. B **86**, 235135 (2012), URL <https://link.aps.org/doi/10.1103/PhysRevB.86.235135>.
- ²⁷ N. Schuch, I. Cirac, and D. Pérez-García, Annals of Physics **325**, 2153 (2010), ISSN 0003-4916, URL <http://www.sciencedirect.com/science/article/pii/S0003491610000990>.
- ²⁸ M. Levin and Z.-C. Gu, Phys. Rev. B **86**, 115109 (2012), URL <https://link.aps.org/doi/10.1103/PhysRevB.86.115109>.
- ²⁹ V. Zauner, D. Draxler, L. Vanderstraeten, M. Degroote, J. Haegeman, M. M. Rams, V. Stojevic, N. Schuch, and F. Verstraete, New Journal of Physics **17**, 053002 (2015), URL <http://stacks.iop.org/1367-2630/17/i=5/a=053002>.
- ³⁰ M. P. Zaletel, Phys. Rev. B **90**, 235113 (2014), URL <https://link.aps.org/doi/10.1103/PhysRevB.90.235113>.
- ³¹ L. H. Santos and J. Wang, Phys. Rev. B **89**, 195122 (2014), URL <https://link.aps.org/doi/10.1103/PhysRevB.89.195122>.
- ³² N. Bultinck, R. Vanhove, J. Haegeman, and F. Verstraete, Phys. Rev. Lett. **120**, 156601 (2018), URL <https://link.aps.org/doi/10.1103/PhysRevLett.120.156601>.
- ³³ J. C. Wang, L. H. Santos, and X.-G. Wen, Phys. Rev. B **91**, 195134 (2015), URL <https://link.aps.org/doi/10.1103/PhysRevB.91.195134>.
- ³⁴ N. Schuch, D. Poilblanc, J. I. Cirac, and D. Pérez-García, Phys. Rev. Lett. **111**, 090501 (2013), URL <https://link.aps.org/doi/10.1103/PhysRevLett.111.090501>.
- ³⁵ D. S. Rokhsar and S. A. Kivelson, Phys. Rev. Lett. **61**, 2376 (1988), URL <https://link.aps.org/doi/10.1103/PhysRevLett.61.2376>.
- ³⁶ F. Verstraete, M. M. Wolf, D. Perez-Garcia, and J. I. Cirac, Physical Review Letters **96** (2006), ISSN 0031-9007, 1079-7114, URL <https://link.aps.org/doi/10.1103/PhysRevLett.96.220601>.
- ³⁷ L. H. Santos, Phys. Rev. B **91**, 155150 (2015), URL <https://link.aps.org/doi/10.1103/PhysRevB.91.155150>.
- ³⁸ R. J. Baxter, *Exact solvable model in statistics mechanics* (Academic Press, London, Inc, 1997).
- ³⁹ D. S. Philippe Di Francesco, Pierre Mathieu, *Conformal Field Theory*, vol. 1 (Springer-Verlag New York, Inc, 1997).
- ⁴⁰ S. C. Morampudi, C. von Keyserlingk, and F. Pollmann, Phys. Rev. B **90**, 035117 (2014), URL <https://link.aps.org/doi/10.1103/PhysRevB.90.035117>.
- ⁴¹ P. Calabrese and J. Cardy, Journal of Physics A: Mathematical and Theoretical **42**, 504005 (2009), ISSN 1751-8113, 1751-8121, arXiv: 0905.4013, URL <http://arxiv.org/abs/0905.4013>.
- ⁴² R. Blumenhagen and E. Plauschinn, Lect. Notes Phys. **779**, 113 (2009).
- ⁴³ P. Ginsparg, arXiv:hep-th/9108028 (1988), URL <http://arxiv.org/abs/hep-th/9108028>.
- ⁴⁴ P. Ginsparg, Nuclear Physics B **295**, 153 (1988), ISSN 0550-3213, URL <http://www.sciencedirect.com/science/article/pii/0550321388902490>.
- ⁴⁵ W. Li, S. Yang, H.-H. Tu, and M. Cheng, Phys. Rev. B **91**, 115133 (2015), URL <https://link.aps.org/doi/10.1103/PhysRevB.91.115133>.
- ⁴⁶ O. M. Sule, X. Chen, and S. Ryu, Phys. Rev. B **88**, 075125 (2013), URL <https://link.aps.org/doi/10.1103/PhysRevB.88.075125>.
- ⁴⁷ C. Castelnovo, S. Trebst, and M. Troyer, arXiv:0912.3272 (2009), URL <http://arxiv.org/abs/0912.3272>.
- ⁴⁸ L. Vanderstraeten, M. Mariën, J. Haegeman, N. Schuch, J. Vidal, and F. Verstraete, Phys. Rev. Lett. **119**, 070401 (2017), URL <https://link.aps.org/doi/10.1103/PhysRevLett.119.070401>.
- ⁴⁹ C. Castelnovo, C. Chamon, C. Mudry, and P. Pujol, Annals of Physics **318**, 316 (2005), ISSN 0003-4916, URL <http://www.sciencedirect.com/science/article/pii/S0003491605000096>.
- ⁵⁰ B. Hsu and E. Fradkin, Phys. Rev. B **87**, 085102 (2013), URL <https://link.aps.org/doi/10.1103/PhysRevB.87.085102>.
- ⁵¹ X. Chen and A. Vishwanath, Phys. Rev. X **5**, 041034 (2015), URL <https://link.aps.org/doi/10.1103/PhysRevX.5.041034>.
- ⁵² H.-H. Tu, Y. Zhang, and X.-L. Qi, Phys. Rev. B **88**, 195412 (2013), URL <https://link.aps.org/doi/10.1103/PhysRevB.88.195412>.